Results in Optics 24 (2026) 101090



Contents lists available at ScienceDirect

Results in Optics

journal homepage: www.sciencedirect.com/journal/results-in-optics





# Gaussian beam evolved structured light techniques for spectroscopy and laser technology

Tomas Ceponis *, Laimonas Deveikis, Kestutis Zilinskas, Eugenijus Gaubas

*Institute of Photonics and Nanotechnology, Vilnius University, Sauletekio ave. 3, LT-10257, Lithuania*

ARTICLE INFO

*Keywords:*
Nonlinear refraction
Structured light beam shaping
Two-photon absorption
*Z*-scan
Photoconductivity
Wave-front curvature

ABSTRACT

Nonlinear refractive index modulation in semiconductors enables lens-less beam shaping and provides a sensitive probe of ultrafast material responses. In this work, the irradiance-dependent transformations of Gaussian laser beams transmitted through a plane-parallel semiconductor are investigated, combining spatial beam-profile mapping with *Z*-scan, two-photon absorption, differential absorption in a pump-probe configuration, and microwave-probed photoconductivity measurements. A ray-optics model is developed to describe externally induced refraction at distances shorter than the Fresnel distance. Their effects, dependent on the radius of wave-front curvature, the distribution of divergence angles, and caustic formation, have been analysed. Experiments in a direct-bandgap semiconductor demonstrate that increasing irradiance determines the evolution of the structured light beam from a Gaussian to a flat-top and ring-shaped profile via refractive index modulation. Microwave-probed photoconductivity transients confirm carrier generation and relaxation, with recombination lifetimes on the order of tens of nanoseconds, linking carrier dynamics to refractive index changes and beam-shape evolution. Comparison of local beam profile mapping with *Z*-scan measurements shows consistent irradiance-dependent refractive index variations while highlighting the different sensitivities of spatially resolved and area-integrated techniques. The results demonstrate that externally induced refraction mapping provides a direct and fast method for evaluating nonlinear refractive index dynamics and enables the controlled formation of flat-top and ring-shaped beams. This approach is applicable to material characterization and to lens-less beam shaping in laser micromachining and photonic applications.

## 1. Introduction

The nonlinear structured-light manipulation now plays a central role in applications ranging from optical communication and microscopy to quantum photonics and ultrafast laser-matter interaction (Sachleen and Forbes, 2026; Buono and Forbes, 2022). The laser beam shaping is an important optical task in various micromachining applications like scribing, PCB drilling, developing of the beam shapers (for the refraction field mapping) in order to optimize conditions of interference near the lens focal plane and forming a variety of profiles: flat-top, doughnut, by making a simple adjustment procedure in switching from one beam profile to another (Dickey, 2000; Laskin et al., 2016). Recent progress in nonlinear optics and structured-light engineering has significantly expanded the possibilities for dynamic beam shaping and wavefront control in photonics (Tu et al., 2026). Modern approaches frequently employ metasurfaces, spatial light modulators (SLMs), diffractive optics, and nonlinear photonic crystals to transform Gaussian beams into flat-top, ring-shaped, vortex, and other structured optical fields (Yan et al., 2025). Programmable beam shaping using digital micromirror devices and nonlinear metasurfaces has further enabled adaptive control of irradiance distributions and harmonic wavefront engineering (Zhao et al., 2026). Despite these advances, most beam-shaping approaches rely on externally fabricated optical structures or imposed phase modulation. In contrast, nonlinear self-action in bulk media provides an alternative route in which the optical field dynamically modifies the refractive index of the material and governs its propagation. In semiconductors, this nonlinear response is especially complex because Kerr nonlinearities, free-carrier generation, two-photon absorption (TPA), band-filling effects, and dispersion of the complex dielectric permittivity may simultaneously contribute to refractive-index modulation. The interplay between diffraction and nonlinear refraction consequently determines beam divergence, wave-front curvature, and transverse beam morphology during propagation.

Nonlinear beam reshaping has attracted increasing interest for laser

* Corresponding author.
*E-mail address:* tomas.ceponis@ff.vu.lt (T. Ceponis).

https://doi.org/10.1016/j.rio.2026.101090
Received 23 February 2026; Received in revised form 29 May 2026; Accepted 15 July 2026
Available online 20 July 2026
2666-9501/© 2026 The Author(s). Published by Elsevier B.V. This is an open access article under the CC BY license (http://creativecommons.org/licenses/by/4.0/).

processing, microscopy, optical trapping, and adaptive photonic systems because flat-top and ring-shaped beams provide controllable energy redistribution and homogeneous irradiation profiles (Schmidt et al., 2024). At the same time, ultrafast pump-probe spectroscopy and nonlinear microspectroscopy have enabled detailed studies of transient refractive index dynamics in semiconductors and quantum materials (Cruz et al., 2024; Minhaeng, 2025). However, in the general case of wave optics, a direct correlation between carrier relaxation dynamics and spatial beam-profile evolution leads to rather complex solutions that indirectly relate changes in refractive index to the integral profiles of transmitted irradiance. Therefore, searching for direct and specific techniques for spectroscopic refractive index profiling and beam shape manipulation is desirable, despite the rather narrow area of their validity.

The lens-less refractive beam shapers are also prospective for beam manipulators in laser-based processing of materials. The refraction field mappers comprise the base of optical design in a family of refractive beam shaping systems, resulting in collimated, low-divergent, speckle-free beams and creating various intensity profiles that might be required for particular laser technologies (Dickey, 2000; Laskin et al., 2016). Consideration of limitations imposed by secondary focusing effects might be important in the formation of caustics due to light rays refracted by curved wave-fronts. The interplay of the non-linear refraction and absorption also complicates analysis of the planar intensity distribution integrals and, thereby, the separation of their parameters without evaluating wave-front curvature modifications. Nonlinear two-photon absorption (TPA) is finding the growing applications in the local sharp focusing of beams for excess carrier induction within various modifications of semiconductor sensors of high-energy radiations, with the purpose to enhance spatial and temporal resolution of ultrafast processes (Kagawa, 2012).

The non-linear phenomena of laser beam self-focusing/defocusing and diffraction have been well understood and comprehensively analysed in a fundamental review Ref. (Akhmanov et al., 1968). A lot of material characterization techniques, such as multi-photon absorption (Dinu, 2003; Garcia and Kalynamaran, 2006; Garcia, 2006; Wherrett, 1984; Garcia and Avanaki, 2012), *Z*-scan (Said et al., 1992; Sharma et al., 2012; Boggess et al., 1986; Van Stryland et al., 1985), have been developed for spectroscopy and mapping of parameters of laser-induced non-linear material characteristics. The advanced development of laser-based techniques, however, requires a deeper analysis of wave-front curvature modifications that cause wide-range changes of beam shape. The ring-shaped laser beams can be generated from scattered laser light using techniques based on rotating ground glass plates, radial gratings, spiral phase plates, axicons, as well as multimode fibers (Reddy et al., 2013; Khonina et al., 2021; Kovalev et al., 2022). These beams find applications in various fields, including optical manipulation, optical tweezers, and microscopy.

The research in this work was addressed to the development of a direct technique for the extraction of refractive index values dependent on the irradiance of Gaussian laser beams, employing analysis of the structured-light beams and wave amplitude mapping. The ray-optics model for the structured light amplitude description in the near field zone has been developed based on the relation of the ray curvature radius $R$ with the refractive index gradient. This approach is valid within the range of Fresnel distances, where direct relations between the optical ray curvature radius $R$ and refractive index exist (Landau et al., 1984). The transforms of the radius $R$ of wave-front curvature in a wide range of the laser beam-induced refractive index modulation magnitude have been studied. The optical ray model of the external refraction has been developed, where the validity of the paraxial approach is proved even for the case of declination from the Gaussian beam shape of spread light. The externally governed changes of ray curvature radius in situations of non-linear focusing and defocusing, followed by beam shape transformations, have been evaluated. The wave-front radius has been linked to this ray curvature based on mutually perpendicular parameters of the tangent and principal normal ascribed to the ray and wave-front curves. The functional variations of the refracted beam divergence angle have been analysed, dependent on the magnitude of the Gaussian distribution of the negative refractive index, over phenomena of self-defocusing or pump-probe technique characteristics observed under laser beam-induced external refraction. The refracted beam broadening or narrowing under an increase in acting irradiance directly indicates the sign of the induced refractive index. It has been demonstrated that inhomogeneity of the divergence angle profile leads to perturbations of the structured-light beams, forming a ring in the limiting case, while the envelope of light rays, propagating within the central and periphery of the incident Gaussian beam, may arrange a caustic of self-focused light at far-field distances. The radius of wave-front curvature, therefore, might change its sign within the lateral coordinates of the incident Gaussian beam. The wave-front curvature-dependent phase shifts should be included in the area integrals when the fluence, integrated over the photon flux, is recorded within the aperture of the photo-detector. The refracted beam profiles have been modelled and illustrated for different signs of refractive index dispersion cases, including non-linear absorption determined lateral distribution profiles. Simulations have been performed and verified for consistency with the experimental characteristics of the external refraction phenomena using a comprehensively examined direct-bandgap semiconductor ZnSe material.

The experimental arrangements for the examination of the non-linear external refraction and transmission characteristics, varying spectrum of excitation and probe beams, are illustrated and discussed. Several combined techniques, such as microwave-probed photoconductivity, two-photon and free-carrier absorption transients at different excitation levels, *Z*-scan and external refraction mapping, have been combined to enhance spatial and temporal resolution in measurements of optical and electrical parameters. The irradiance-induced beam reshaping in bulk ZnSe has been investigated. Unlike conventional beam-shaping systems based on metasurfaces or SLMs, the present approach demonstrates a dynamically controllable, lens-less transformation of Gaussian beams into flat-top and ring-shaped profiles through self-induced Gaussian refractive-index gradients. A ray-optics-based analytical model is developed to describe curvature radius evolution, divergence angle redistribution, and caustic formation during the propagation of Gaussian beams. Furthermore, the combined optical and electrical measurements establish a direct relationship between free-carrier dynamics, nonlinear refractive index modulation, and beam-profile evolution in ZnSe.

## 2. Analysis of the external refraction phenomena induced by Gaussian beams

The non-linear effects of light self-action within materials alter the angular spectrum of the propagating wave. Propagating waves are usually analysed using the slowly varying field amplitudes, where their deviation due to the non-linearity of the medium, and to diffraction appears. There, the changes across the beam are assumed to be faster than those along the beam. Considering the first-order terms in the nonlinear polarization, a simplified equation then describes the effects of self-actions. Various nonlinear phenomena are generally considered using fundamental wave equation governing light propagation in a nonlinear medium (Minhaeng, 2025), where solutions for the electric field (under polarization of the medium) describe the response of the medium to the input electric field, and systematically models the nonlinear optical response, especially under intense illumination where the material response deviates from linearity. The expansion of the complex dielectric permittivity in powers of the wave field determines variations of field amplitude $A$. The plane wave with wave vector $\boldsymbol{k}$ is characterized by the complex wave field amplitude and the eikonal $s$ (wave front) as $A = A_0\exp(-i\boldsymbol{k}s)$. Inserting the expression of this complex amplitude $A$ in the wave equations, terms linked to the “forces” of

the nonlinear refraction and the diffraction, respectively, appear. The solution of this system of equations would also determine the paths of the optical rays. Such a solution depends on the initial phase front and on the form of the amplitude profile of the wave. However, it is impossible to obtain analytical solutions in general form for some arbitrarily specified initial profiles of $s(z = 0, r)$ and $A(z = 0, r)$. Therefore, digital solutions of the Maxwell equations or solutions based on the integral transforms (for instance, Hankel type) (Said et al., 1992; Rice, 2020; Sheik-Bahae et al., 1990) should be applied. Usually, interference analysis requires quite intensive and cumbersome mathematical computations. However, the latter considerations are quite complicated, indirect and far from practicality in the estimation of the induced refractive index $\Delta n$ values as well as their profiles, thereby being impractical for engineering purposes and fast material characterization techniques.

Formation of ring-shaped beams in semiconductor materials by varying the intensity of the Gaussian beam-induced refractive index distribution had been demonstrated in (Van Stryland et al., 1985; Vaitkus et al., 1986a; Vaitkus et al., 1987). However, these demonstrations lacked the precision of mapping detectors and modern laser instrumentation, as well as suitable models to relate profiles of the refracted beam distribution with local changes of material parameters. Nevertheless, the observed phenomena enable to make generators of ring-shape beams of variable duration (up to ultrashort pulses) by lensless manipulation of modulations of the refractive index in semiconductor materials. A special trend in the generation of ring-shaped beams is based on consideration of scattered Laguerre-Gaussian (LG) as well as Bessel-Gaussian (B-G) beams, where the latter B-G's may propagate without an apparent spreading due to diffraction. Thereby, the state-of-the-art problems of the structured light involve engineering of the precise control of the amplitude, phase, polarization, and spatiotemporal properties of the propagating waves, which are extensively studied now for both scientific and applied purposes (Minhaeng, 2025). There, amplitude modulation has enabled the generation of various transverse-mode optical fields, such as Gaussian, Hermite-Gaussian (HG) and LG beams, while phase and polarization modulations have yielded optical vortices and vector beams (Minhaeng, 2025). Solutions based on structured light find broad applications in quantum communication, high-resolution imaging, and laser processing.

### 2.1. Model developed on the basis of the ray optics approach

The particular solutions, represented by the curvature radii of the incident waves, can be obtained by solving the Helmholtz equation (Rice, 2020) in the Fourier domain, where one set of solutions is the plane waves. However, plane waves represent an idealization, which is impossible because of the infinite amount of energy required to generate such plane waves. The simplest approximation describing a beam of finite size is the Gaussian beam. Gaussian beams retain their shape as they propagate in free space. However, because of its finite size, diffraction broadens the Gaussian beam. The Gaussian beam solutions with different finite transverse radius $w$ in $k$-space and real space behave as if they represent beam propagation along the z-axis with different imaginary z-component $Z_R$ of the Rayleigh length. However, the Gaussian beam approach is applicable when changes in the curvature radius do not lead to deviations from the Gaussian beam shape. Nevertheless, the Gaussian beam curvature radius has been analysed in the presented modelling to account for variations in the probed beams.

In the nonlinear medium (with non-linear terms of dielectric permittivity $\varepsilon_2 \neq 0$), the generalization of the solutions, including variable wave-front radius of curvature, is described by the system of parameters (Akhmanov et al., 1968):

$$s = \frac{r^2}{2} R(z) + \varphi(z) \tag{1a}$$

$$A_0^2 = \frac{E_0^2}{f^{1+m}(z)} \left[1 - \frac{2r^2}{a^2 f(z)}\right] \approx \frac{\left(E_0 \exp\left(\frac{-r^2}{a^2 \bullet f(z)}\right)\right)^2}{f^{1+m}(z)}, \tag{1b}$$

where $R(z)$ is the radius of curvature, $\varphi(z)$ is the addition to the eikonal due to a change in the wave propagation velocity, and $f(z)$ is the dimensionless width of the beam, $E_0$ is the field on the beam axis, while $a$ is the beam width. The main objective in the description of variable curvature radius, which governs beam shape, is to find a solution for the $f(z)$ dimensionless width of the two-dimensional ($r$-$z$ plane and $m = 0$, satisfying the initial conditions $\varphi(0) = 0$, $f(0) = 1$) beam based on geometrical/ray optics approaches that lead to acceptable coherence with experimental characteristics of the external refraction phenomena. The radius $R$ of wave-front curvature is directly related to the complex curvature $q$ of the Gaussian beam and Rayleigh length $Z_R$ as $q^{-1}(z) = R^{-1}(z) + iZ_R^{-1}(z)$ (Sheik-Bahae et al., 1990; Znak, 2019; Alda, 2015). The Rayleigh length here defines the Gaussian beam spread related to diffraction, while the radius of curvature includes refraction. Therefore, transforms of the radius $R$ of wave-front curvature under various modulation mechanisms of material complex refractive index play an important role in grounding different techniques of material characterization as well as laser beam manipulations.

Manifestation of various mechanisms in changes of the sign and magnitude of the non-linear refractive index is usually dominated by the effects of bound and free carriers. However, competition of different mechanisms acting on refractive and extinction index dispersion (Hadi et al., 2021) complicates applications of material characterization techniques. Dispersion of the nonlinear refraction in solids and its role in the characteristics of the $Z$-scan technique is well reviewed in a set of articles (Said et al., 1992; Sheik-Bahae et al., 1990; Sheik-Bahae et al., 1991a; Sheik-Bahae et al., 1991b; Sheik-Bahae et al., 1994). However, the approach of beam-shape invariance is employed for modelling $Z$-scan characteristics, while the radius of the wave-front curvature can be significantly modified even within the paraxial range of Gaussian beams.

In the models presented in this research, the curvature radius modifications are linked to refractive-index gradients within the material. This relation to ray optics has been derived in (Landau et al., 1984) and is widely exploited in the solution of problems of gravitational fields, local gauge theory (Hadi et al., 2021), non-linear optics and computational seismology (Madrid, 2008), etc. This refractive index $n(r)$-curvature radius ($R$) relation can be expressed as (Landau et al., 1984):

$$\frac{\overrightarrow{N}}{R} = \boldsymbol{grad}\ (\boldsymbol{ln}(\boldsymbol{n}(\boldsymbol{r}))) \equiv \frac{\overrightarrow{\nabla}\boldsymbol{n}(\boldsymbol{r})}{\boldsymbol{n}(\boldsymbol{r})}, \tag{2}$$

where $n(r)$ is the spatial coordinate ($r$) dependent refractive index of medium, $\overrightarrow{N}$ represents a principal normal of the basic triangle of differential geometry, (Fig. 1). Thereby, scalar quantity $R^{-1}$ is determined by a dot product of $\overrightarrow{\boldsymbol{N}} \bullet \boldsymbol{grad}(\boldsymbol{n}(\boldsymbol{r}))$. This result tells that the rays are bent in the direction of increasing refractive index (Landau et al., 1984). Also, the group velocity of ray propagation appears along the unit vector of the tangent derivative. Then, light intensity is related to the Poynting vector (averaged over time in a steady-state regime). The transverse origin of the electromagnetic waves determines the location of the wave field vector within the normal plane, based on $\overrightarrow{N}$ and $\overrightarrow{B}$ vectors. Light of the invariable intensity and group velocity, thus, propagates along the tangent vector (Landau et al., 1984). Owing to mutually perpendicular planes of tangent fluxions related to wave-fronts and rays, kept among $\overrightarrow{N}$, $\overrightarrow{T}$ and $\overrightarrow{B}$ vectors, ascribed to optical ray and wave-front, seems to be valid in both ray and wave optics cases. Additionally, light propagation along the ray determines rotation of the light polarization vector within the normal plane (determined by $\overrightarrow{N}$ and $\overrightarrow{B}$) specified by radius of torsion (Landau et al., 1984).

To simplify the consideration of different regimes and to simulate the

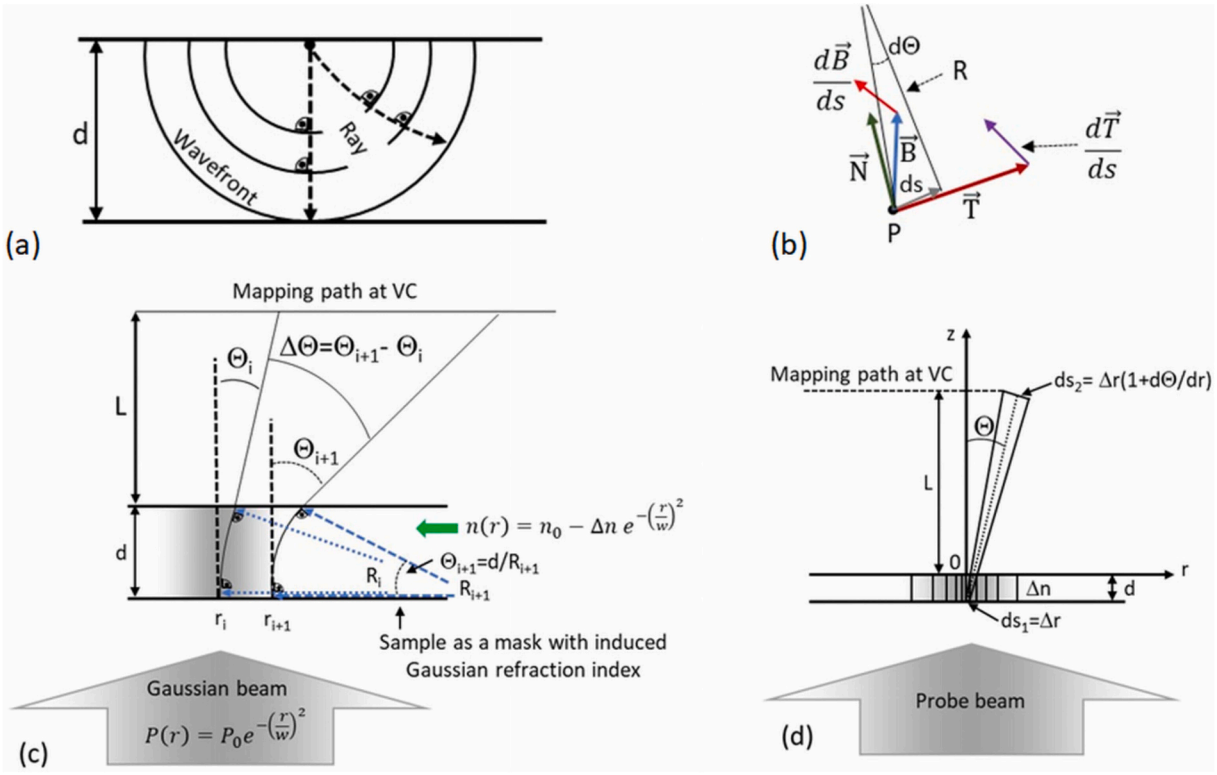


**Fig. 1.** (a) Interface between light ray-path and variations of the wave-front curvature radius. (b) Relations among parameters that specify a wave-front curvature radius. The main elements and planes of the differential geometry: $\vec{T}$ is a vector of tangent derivative for a spatial curve with length differential $ds$ at point $P$, $\vec{N}$ is a vector of principal normal, $\vec{B}$ is a bi-normal. (c) A scheme of the model for sketching of the intensity distribution within the refracted beam, based on the bent ray bundles (stream tubes (Ihrke et al., 2007)), the lateral minute spans of which determine a differential one-dimensional width of ray bundles, and $r_{z,i}$ vary with longitudinal distance $z$ relative to the video camera (VC). (d) The intensity law of geometric optics is based on the product of 1D area and differential irradiance, which is constant along a tube of rays.

output field structure changes, a mask approximation is employed here to present the input of the refractive index shape initially induced by the excitation laser beam within the medium under examination. It is assumed that a Gaussian shape profile of material refractive index modulation $\Delta n \times \exp(-r^2/w^2)$ is externally induced. The material refractive index $n(r)$ with its unperturbed value $n_0$ depends on the sign of the induced refractive index, as:

$$n(r) = n_0 \pm \Delta n \times \exp\left(-\frac{r^2}{w_0^2}\right). \tag{3}$$

Here $\Delta n$ is the absolute magnitude of the induced refractive index modulation at the centre ($r = 0$) of a Gaussian beam of initial ($z = 0$) radius $w_0$. In the case when the plain wave propagates through a medium and reads this induced refractive index profile, the output rays or wave-fields experience a distortion of their path according to the medium refractive index determined (Eqs. (2) and (3)) curvature radius. It can be deduced from Fig. 1(b) that the radius of curvature is related to the wave-speed gradient and ray divergence angle $\Theta$ (Landau et al., *1984*; Rice, *2020*; Alda, *2015*).

The angle $\Theta$ of the ray divergence, ascribed to the external refraction on the induced Gaussian profile with curvature radius $R_n(r)$ in the plane-parallel sample of thickness $d$ (Fig. 1(d)), at its exit surface can be estimated using the relation:

$$\Theta_n(r) \approx \frac{d}{R_n(r)}. \tag{4}$$

The sign of curvature radius is determined by the dispersion mechanism prevailing in modulation of the refractive index: the positive values of $R > 0$ are inherent for defocusing ($\Delta n < 0$) region of the excited material, while multi-focusing is governed by the region of the negative values ($R < 0$, i.e. $\Delta n > 0$) of wave-front curvature radius. The ray curvature radius is evaluated (using Eqs. (2 and 3)), as follows:

$$R_{n-}(r) = \frac{w_0^2}{2r}\left[\frac{n_0}{\Delta n}\exp\left(\frac{r}{w_0}\right)^2 - 1\right] > 0, for\ \Delta n < 0, \tag{5a}$$

and

$$R_{n+}(r) = -\frac{w_0^2}{2r}\left[\frac{n_0}{\Delta n}\exp\left(\frac{r}{w_0}\right)^2 + 1\right] < 0, for\ \Delta n > 0. \tag{5b}$$

The non-monotonic variation of the ray distortion angles $\Theta(r)$, dependent on radial coordinate ($r$), appears for both focusing and defocusing cases owing to the features of the Gaussian shape. The appearance of the extremum at about $r \cong 0.707 w_0$ is inherent for the Gaussian profile (Fig. 2).

Moreover, the simulated profiles of total and refraction caused of ray divergence angles $\Theta_s(r) \sim \Theta_R(r)$ variations, illustrated in Fig. 2, confirm that for the induced Gaussian refractive index profile, the changes of the ray/wave-front curvature radius are mainly localized within the extent of the intrinsic laser Gaussian beam radius $w_0$ (ascribed to the incident beam), where an extremum of the divergence angle is obtained. There, the refraction angle variations, dependent on $r$ and $\Delta n/n_0$, show a peak at threshold $r_{thr}$ values of radial coordinates $r_{thr} \cong w_0[(1 - \Delta n/n_0)/(2 - \Delta n/n_0)]^{1/2} \cong 0.707 w_0$. This enables the assumption of paraxial validation across varied profiles of refracted beams, excluding far-field cases that appear in caustics due to the intersection of central-region rays with peripheral ones within the probe beam, which reads the induced refractive index profile. Thus, the basics of the light rays/wave-front curvature radius model are valid within the near field (limited by

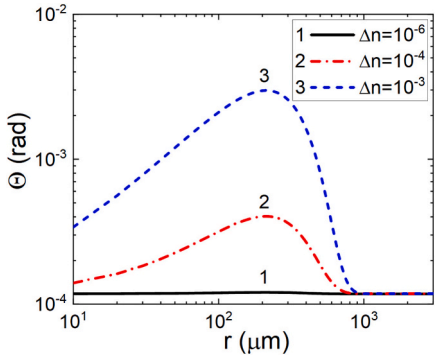


**Fig. 2.** Simulated variations of the divergence angle using the set of parameters: $z = 10^5$ μm, $w_0 = 300$ μm, $n_0 = 2.7$, $\lambda = 0.532$ μm, $d = 3000$ μm and $\Delta n(z = 0)$ varied in the range of $10^{-6}$–$10^{-3}$.

Fresnel distance) when the detector is placed at distances $z$, where diffraction on the aperture of $2w_0$ can be neglected for distances $z < R_{df} = \pi[n_0 - \Delta n \times \exp(-r^2/w_0^2)]w_0^2/\lambda$. This, consequently, is valid when the refractive index modulation $\Delta n$ is small relatively to its equilibrium value $n_0$, i.e. for regimes of $n_0/\Delta n >> 1$. It can be implied that $R_{n0}(r) = \infty$ in the case of the absence of a refractive index gradient, which corresponds to a flat wave.

In the case of self-action of the Gaussian beam, the reading rays also experience diffraction, determined by the Rayleigh curvature radius (Rice, 2020; Alda, 2015).

$$R_G(z) = z\left(1 + \left(\frac{Z_R}{z}\right)^2\right) \tag{6a}$$

ascribed to Gaussian beams with $Z_R$ Rayleigh range. The diffraction then determines the divergence half angle (Alda, 2015).

$$\Theta_{df}(r) \approx \frac{w_0}{R_G(r, z, w_0)} \approx \frac{\lambda}{\pi w_0} \tag{6b}$$

There, diffraction divergence can be treated as a result of the action of a defocusing lens with focal length $R(z)$ (Akhmanov et al., 1968). Obviously, the divergence angles should be summarized ($\Theta_s \cong \Theta_{df} + \Theta_{n-}$ with $R_s^{-1} \cong R_n^{-1} + R_{df}^{-1}$) for the defocusing of beams, while the difference ($\Theta_s \cong \Theta_{df} - \Theta_{n+}$ with $R_s^{-1} \cong R_{df}^{1} - R_{n+}^{-1}$) should be analysed in the self-focusing case. These relations lead to the complicated characteristics of the total divergence angle $\Theta_s(r,z,w_0)$ and total curvature radius $R_s(r,z,w_0)$.

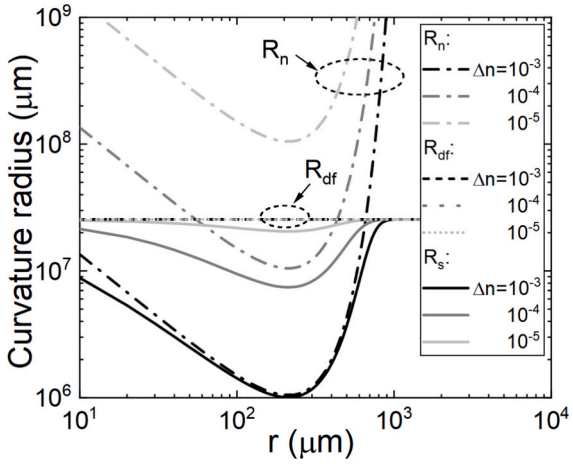


**Fig. 3.** Simulated variations of the refraction as well as the total curvature radii (measured in μm) dependent on the externally induced refractive index of the amplitude $\Delta n$ as a function of the radial coordinate $r$.

The radial coordinate-dependent total curvature radius ($R_s$) and its components ($R_{df}$ and $R_{n-}$) are illustrated in Fig. 3 for the case of nonlinear self-defocusing of Gaussian beams propagating through a plane-parallel mask with an induced Gaussian profile of refractive index modulation. The simulations of these curvature radii have been performed for the same (as in the case of Fig. 2) set of parameters: $z = 10^5$ μm, $w_0 = 300$ μm, $n_0 = 3$, $\lambda = 0.532$ μm, $d = 3000$ μm and $\Delta n(z = 0)$ varied in the range of $10^{-6}$–$10^{-3}$.

It can be deduced from Fig. 3 that the total curvature radius is rigorously positive over the entire range of radial coordinates, indicating defocusing due to both refraction and diffraction. However, the divergence angles are mainly governed by the induced refraction for significant $\Delta n(z = 0) > 10^{-6}$ values in the range of $r < 2.5w_0$. Moreover, the impact of diffraction determined modification of the total refraction radius can be significantly suppressed in the range of the enlarged divergence angle (e.g. for $\Delta n(z = 0) > 10^{-4}$) at $r \approx 0.7w_0$. Nevertheless, only a minimal diffraction angle dependence on modulation of the refractive index ($\Delta n$) appears for the range of $r < 2w_0$ due to wavelength-dependent Rayleigh length within the material, while the diffraction dominates in modification of the total curvature radius for the range of radial coordinates $r > 3w_0$.

The self-focusing phenomena are widely discussed in the review Ref. (Akhmanov et al., 1968). Therefore, in this article, the defocusing phenomena will be mainly considered.

### 2.2. Irradiance distributions in the refracted beams

At the sample entrance plane $z = 0$, the induced refraction angle variations with radial coordinate $r$ are related to its variation either at the sample exit surface $z = d$ or at the detector plane $z = L$ and described through transformation of the coordinates $r_z$ ascribed to a location of the same ray ($i$) within the screen/detector plane as:

$$r_{z,i} = r_i + z\Theta(r_i). \tag{7}$$

Actually, the changes in the ray curvature radius appear only within a plane-parallel sample of the material with an induced refractive index profile. These changes are ceased just on the exit surface of the sample, while further, in free space, these rays propagate retaining a fixed divergence angle (as illustrated in Fig. 1(d)), dependent on the radial coordinate at the entrance plane. In the ray approach, the beam intensity variations at distance $z$ are routinely represented (Ihrke et al., 2007) by changes of the ray bundle tube area (a bundle width constructed of the adjacent rays in the case of a two-dimensional $r$-$z$ beam). This width is then represented as:

$$\Delta r_{z,i} = (r_{i+1} - r_i) + z[\Theta(r_{i+1}) - \Theta(r_i)]. \tag{8}$$

Applying the intensity law of geometric optics (Ihrke et al., 2007), which along $z$ is then obtained as: $P(z)dr(z) = P(z = 0)dr(z = 0)$. Based on the model sketch, illustrated in Fig. 1(d), the transformation of the irradiance is then represented as:

$$P(z) = P(z = 0)\frac{dr(z = 0)}{dr(z)} = P(z = 0)\left[1 + z\frac{d\Theta}{dr}\right]^{-1}. \tag{9}$$

This expression indicates that the product of the area and differential irradiance ($P$) is constant along a tube of rays, and assuming this area is infinitesimal, the transformation relation for intensity changes along z is then obtained: $P(z)dr(z) = P(z = 0)dr(z = 0)$.

In the case of self-refraction of Gaussian beams, attributed to the induction of free carriers, Eq. (9) acquires the form:

$$P(z, r) = P_0(z = 0)\exp\left(-\frac{r^2}{w_0^2}\right)\left[1 + z\frac{d\Theta}{dr}\right]^{-1}. \tag{10a}$$

For the pump-probe regime, the refracted beam intensity distribution is described by the expression:

$$P(z,r) = P_0(z=0)\left[1+z\frac{d\Theta}{dr}\right]^{-1} \tag{10b}$$

where

$$\left[1+z\frac{d\Theta}{dr}\right]^{-1} = \left\{1+\left(\frac{2zd}{w_0^2}\right)\frac{\left[\left(\frac{n_0}{\Delta n}\right)\exp\left[\left(\frac{r}{w_0}\right)^2\right]\left(1-2\left(\frac{r}{w_0}\right)^2\right)-1\right]}{\left[(n_0/\Delta n)\exp\left[\left(\frac{r}{w_0}\right)^2\right]-1\right]^2}\right\}^{-1}, \tag{10c}$$

and probe beam irradiance is invariable, i.e. $P_0(z=0) = \text{const}$. However, in the general case, the refracted beam intensity distribution should be analysed using the generalised expression

$$\left[1+z\frac{\partial\Theta}{\partial r}\right]^{-1} = \left\{1+z\,\frac{\partial}{\partial r}\left[\frac{d}{R_s(r,\Delta n)}\right]\right\}^{-1}. \tag{11a}$$

Indeed, the obtained ratio of the ray tube base (1D) area change is

$$\left[\frac{dr(z=0)}{dr(z)}\right] = f(z)^{-1} = \left[1+z\frac{\partial\Theta}{\partial r}\right]^{-1} = \left[1+z\frac{\partial(d/R_s(r,z,\Delta n))}{\partial r}\right]^{-1}. \tag{11b}$$

In the ray approach, Eqs. (9) and (10b) represent a quantity equivalent to the $f(z)$ dimensionless width of the beam within the wave-fronts approximation, where, in the case of the two-dimensional beam: $r$-$z$, $m = 0$ (Akhmanov et al., 1968).

The radial coordinate-dependent changes of the divergence angle, $\sim\partial/\partial r[d/Rs(r,\Delta n)]$ are specifically related to the peculiarities of the Gaussian shape variations. These variations can be highlighted using the second fluxion $\partial^2/\partial r^2[d/Rs(r,\Delta n)]$, those clarify the extremal zones of functional characteristics of the divergence angle, as illustrated in Fig. 4 (a). The divergence angle rising functional ranges can be implied for the zones $r < w_0$, while clear ranges of the divergence angle minimum, indicated by $\partial^2/\partial r^2[d/R(r,\Delta n)] > 0$, can be observed in zones of $r > w_0$.

Additionally, the range of negative values for the refraction-dominated total inclination angle is evident (Fig. 4(b)), indicating the formation of a ray-gathering lens. Such a phenomenon of the sign varied inclination angle changes emerges when the right-side rays (at $r_{i+1}$ within a 1D ray tube) are less bent than that of the left-side ones (at $r_i$, Fig. 1(c)) due to a negative derivation of the sinking wing of the Gaussian profile (Fig. 2). Such a behaviour of inclination angles (Fig. 4 (b)), those comprise the 1D ray tubes of varied base area ($dr$ length in 1D), indicate focusing of rays when $\partial^2/\partial r^2[d/Rs(r,\Delta n)]$ becomes negative for the specific range of radial coordinates $r$. This indicates the formation of the local caustics within the latter ranges of the negative values of derivatives of the total inclination angle curves, those constitute the sides of a 1D-2D ($r$-$z$) ray tube. The total inclination angle changes are mainly caused by variations in the curvature radii, forming sides of the ray tubes. Also, the characteristics $\partial^2/\partial r^2[Rs(r,\Delta n)]$ vs $r$ might be useful for identifying the ranges of radial coordinates where the rays would be focused.

The modifications discussed above of the total inclination angle determine the refracted irradiance radial distribution profiles with the enhancement of $\Delta n$ is illustrated in Fig. 5(a). These irradiance distribution profiles have been simulated by combining Eq. (10) and varying the induced refractive index changes $\Delta n/n_0$.

The transmitted irradiance distribution profile changes its shape, under an increase of $\Delta n$, where starting from the Gaussian profile, it evolves through a square wave profile to the ring-like beam cross-sectional projection. This effect of beam shape transformation can be explained by the aforementioned features of the refraction angle and the spreading of the minute bundles of small differential widths. Media with a specific lateral gradient of refractive index, induced by a Gaussian laser beam, act like a lens with a variable focal length.

Threshold focus length $L_{thr}$, indicating genesis of the beam caustic due to the intersection of the adjacent ray bundles, is specified by the vanishing of the ray tube base at the mapping plane, i.e. when $dr(L_{thr}) = \left[1+L_{thr}\frac{\partial\Theta}{\partial r}\right] \le 0$. The latter measure of the vanishing width (at $z = L_{\text{thr}}$) of the ray tube can be estimated using either the spot size of diffraction limited beam or pixel size (Saleh and Teich, 2019). A tentative measure of mapped spot size can be estimated using Eq. (11) with $dr(z=0) \cong \lambda$. There, wavelength $\lambda$ would represent an elemental period over width changes in the caustic zone, when assuming the diffraction-limited partial beams that comprise the ray tubes. Here, the negative $\partial\Theta/\partial r \cong d \times \partial/\partial r[1/R_s(r,\Delta n)]$ values would imply action of the focusing lens, similarly to a curvature radius sign in the nomenclature of lens parameters.

The simulated threshold length variation with beam radial coordinate is illustrated in Fig. 5. Threshold focus length $L_{\text{thr}}$, separates three ranges related to $r$: the first range (I) of paraxial defocusing constructed of the diverging ray tubes, the second range (II) responsible for profiles from square-wave to ring-shape ones formation due to the strong bend of rays and decrease of intensity within paraxial beam zone, and the third range (III) of multi-focusing due to intersection of strongly bent central rays with periphery ones, where caustic appears at $L > L_{thr}$ (Fig. 5(b)). The formation of negatively inclined boundaries of ray tubes leads to the appearance of a focusing lens, where the negatively inclined divergence angles act as the negative curvature radius zones, which can be deduced from Fig. 5(b). There, the range of radial coordinate $r$ values between the negative and positive peaks determines the built-in focusing lens within the spreader material sample. Appearance of the opposite inclination of the propagating rays for the periphery zone (Figs. 4(b) and 5(b)) relative to that of the paraxial region leads to the improper expression for description of the ray tube base width in Eqs. (9) and (11). Therefore,

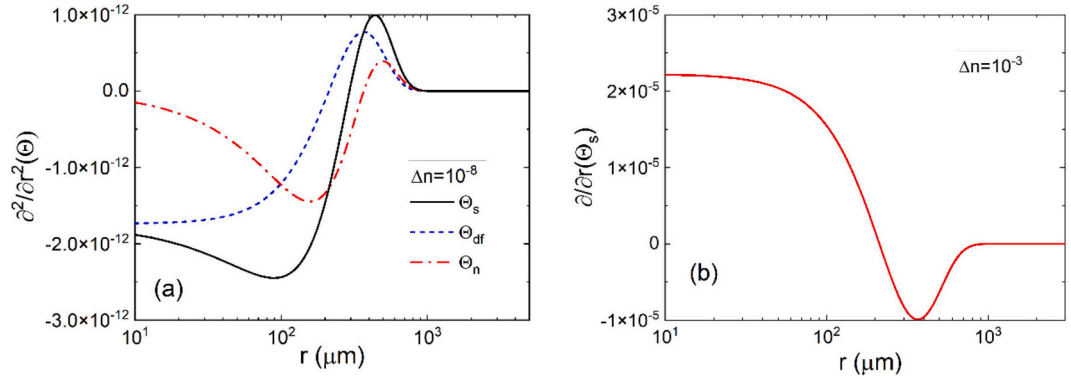


**Fig. 4.** (a) The radial coordinate ($r$) dependent locations of the extrema of the divergence angle ascribed to the total curvature radii changes and that related to diffraction and refraction, respectively. (b) The ranges of the negative values for the refraction-dominated total inclination angle appear.

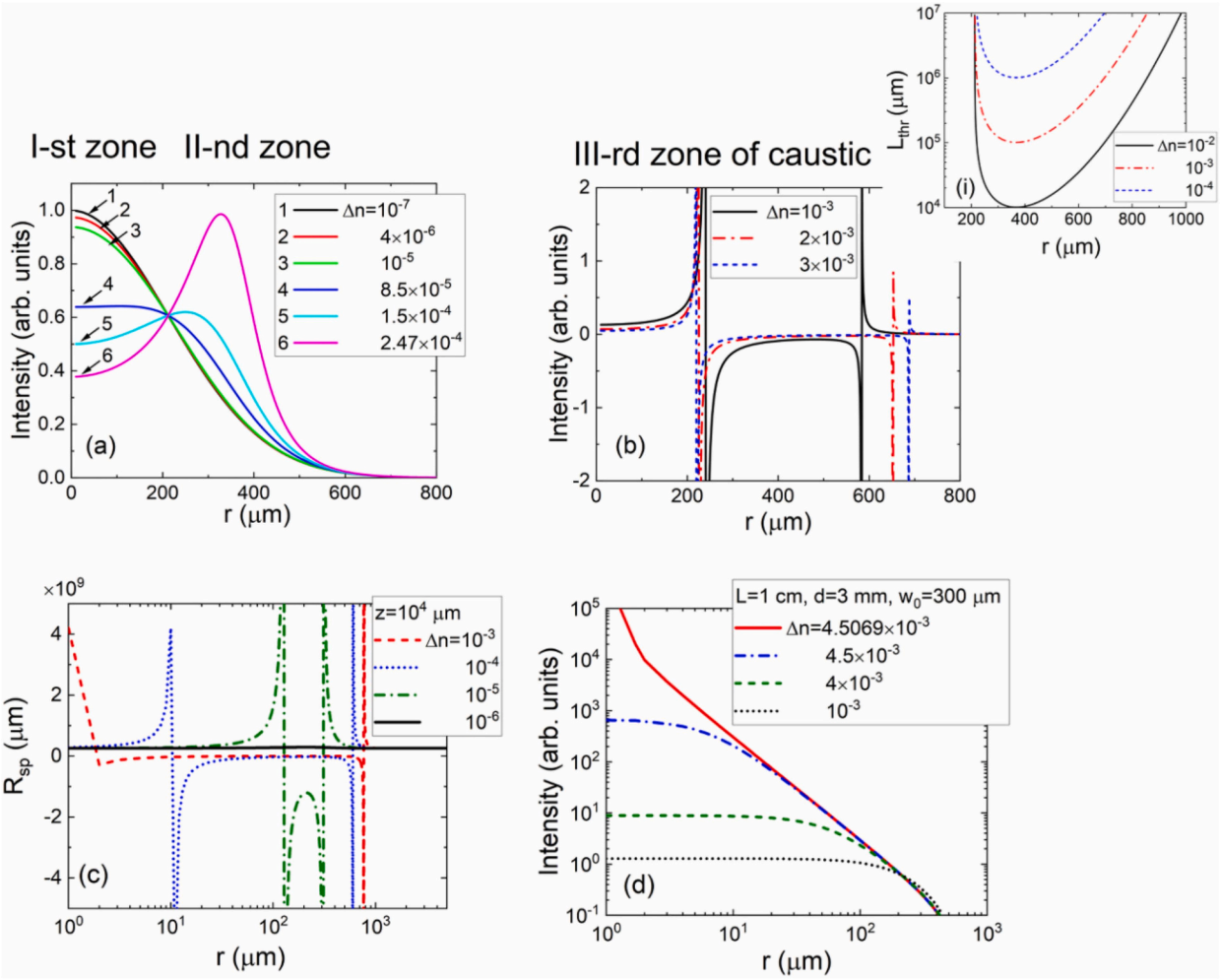


**Fig. 5.** (a) Simulated evolution of the intensity distribution in the defocusing radial profiles with enhancement of $\Delta n$ in the range out of the caustic. (b) Three zones (indicated in figures a and b) of the refraction beam formation can be considered: zone I of nearly invariable shape Gaussian beam with $R_{n\text{-}} > 0$, zone II of varied beam shape which is transformed to a flat-top and ring-like beam with $R_{n\text{-}} < R_{df}$, and zone III of caustic appearance with $R_s < 0$, however, $L_{thr} > 0$. In the inset (i) for graph (b), the simulated threshold range varies dependently on the induced refractive index approaching to the caustic $R_{n\text{-}} < 0$ and $f(z)^{-1} < 0$. In (c), the similar zones for the case of self-focusing can be predicted by analysing the total curvature dependences on the radial coordinate and the refractive index values $\Delta n$ at the centre of the Gaussian profile for fixed mapping position ($z$). It can be deduced from (c) that for the largest refractive index values, the total curvature radius appears to be negative in the range of $0 < r \leq w_0$, indicating the prevailing of focusing in the paraxial range of the beam. For this focusing regime, the intensity enhancement in the central beam area is very sensitive to changes in $\Delta n$ value when approaching the sharp focus range (d).

direct application of Eqs. (9) and (10) for the simulation of intensity distribution within the caustic zone would lead to an infinite increase of intensity in this region (due to $dr(z) \to 0$ in Eq. (11(b)), owing to the rapid increase of term $\left[1 + z\frac{\partial\Theta}{\partial r}\right]^{-1}$ with negative $z\frac{\partial\Theta}{\partial r}$). However, the intersection of the partial ray tubes, with inverted derivations in the evaluation of ray tube sides, wrongly shows singularities in the intensity variation of defocused beams at the boundaries of the caustic zone. In the case of refraction-caused focusing, the competition of diffraction and refraction determined curvature radii might produce radial locations with unperturbed refractive index ($n_0$), which creates collimated (waveguided) beam sectors. The zones of focusing and defocusing can be predicted by analysing the total curvature dependences on radial coordinate and refractive index values $\Delta n$ at the centre of the Gaussian profile (Fig. 5(c)) for fixed position ($z$). It can be deduced from Fig. 5(c) that for the largest refractive index values, the total curvature radius appears to be negative in the range of $0 < r \leq w_0$, indicating the prevailing focusing in the paraxial range of the beam. For the focusing regime, the intensity enhancement in the central beam area is very sensitive to $\Delta n$ value changes approaching the sharp focus range (Fig. 5 (d). Self-focusing, collimating and intersection of the partial ray tubes in the case of the negative curvature induced radii wrongly include singularities in the intensity variation of self-focused beams at the boundaries of different zones (Fig. 5(c)). Pure self-focusing could be observed only in the notably narrow range of the $\Delta n$ value diapason, as illustrated in Fig. 5(d). There, the nearly flat-top, initially Gaussian-shaped beams show a reduction in the radial width of the flat-top range with increasing $\Delta n$ and focusing to about a few μm spot. The intensity enhancement is very sensitive to $\Delta n$ value changes approaching the sharp focus range.

### 2.3. *Simulations of the irradiance distribution of the refracted beams inherent for various mapping regimes*

For the self-defocusing characteristics discussed above, the externally induced Gaussian-shaped refractive index profiles are assumed to be synchronously probed using a Gaussian beam irradiance, matched to the refractive index modulation profile. The supplementary information on the spectral and irradiance-dependent characteristics of the material and the acting beams can be extracted by employing a pump-probe regime. There, a wide probe beam would be preferable, as it does not

modify the induced refractive index profile. Such a method approaches the probe regime with a plane wave. Then, the spectral, temporal and intensity characteristics of the refractive index modulation and the induced profile scanning can be purposefully modified. A wide probe beam can be achieved by defocusing/collimating the emission of the additional laser beam.

The simulated changes in the induced Gaussian refractive index profile, dependent on the amplitude of the induced refractive index ($\Delta n$) and mapped by a plane wave probe, are justified by choosing the relevant location of the mapping plane, which should be less than the threshold distance $L_{thr}(r,\Delta n)$. This distance for the induced profile of $w_0$ width comprises a few tens of cm. The transmitted irradiance level is set by the probe, whose unperturbed value is normalized to a unit. The inclination of rays, caused by modified curvature radius within the paraxial range, governs a decrease in the recorded probe irradiance ascribed to the paraxial zone. Due to conservation of distributed energy (or density of photons within a 1D (in $r$) ray-tube), the reduction of irradiance is balanced by a significant increase and narrowing of the peak in the vicinity, however, out of the caustic zone. The simulated profiles in Fig. 6 hint on possibility to significantly amplify the specific spatial range of a homogeneous beam, whose location ($r \geq 0.7w_0$), intensity and spatial profile could be governed by the external Gaussian beam intensity, i.e. by the induced $\Delta n$ value.

The fast nonlinearity ascribed to bound electrons is related to the third-order susceptibility derived using Kramers- Kronig relations (Hutchings et al., 1992), and it is dependent on the incident irradiance $P$. The free-carrier nonlinearity appears through the consequently induced third and fifth-order dielectric susceptibilities. The electronic Kerr effect in semiconductors may dominate at extremely low irradiance levels. Modulation of the irradiance and thus radial coordinate dependent refractive index is expressed by incorporating the

$$n(P,r) = n_0 \pm \Delta n = n_0 \pm \frac{n_2}{2}|E|^2 = n_0 \pm \gamma P, \tag{12}$$

where $E$ is the peak amplitude of the incident electric field, and $P$ denotes the irradiance. The free-carrier-determined refraction term $\Delta n_{FC}$ is expressed in phenomenology through a coefficient $\sigma$, indicating the single carrier pair ascribed refractive index modulation, and density of the induced electron-hole pairs $\Delta N_{eh}$, as $\Delta n_{FC} = -\sigma \Delta N_{eh}$. The dispersion of the free-carrier-induced refractive and extinction indexes is routinely described using the Drude model, where the change in the real and imaginary constituents of the refractive index due to free carriers is described (Hutchings et al., 1992; Soltani and Soref, 2015). Other mechanisms related to local heating of the material, to heat locally generated sound waves, and other effects appear as a result of relaxation of the fastest processes. Their impact on the modulation of refractive index might be included using inherent material parameters such as the thermo-optic coefficient ($n_T = dn/dT$) which describes the temperature-modulated refractive index $\Delta n_T = -\sigma_T \Delta T$. For ZnSe crystals, values of this $\sigma_T$ coefficient are in the range of $10^{-4}$ $K^{-1}$ and depend on wavelength and temperature due to thermal lattice expansion and changes in the semiconductor's band structure. Moreover, the value of the thermo-optic coefficient in ZnSe is positive, therefore the appearance of the $\Delta n_T$ impact should lead to the reduction of the free carrier-induced modulation of refractive index (with $\Delta n_{FC} < 0$). Such an effect should be clearly observable within transients of the mapped refraction images, especially in the range of elevated irradiances. However, the impact of the thermal effects in ZnSe was not observed within the range of applied irradiances in our experiments.

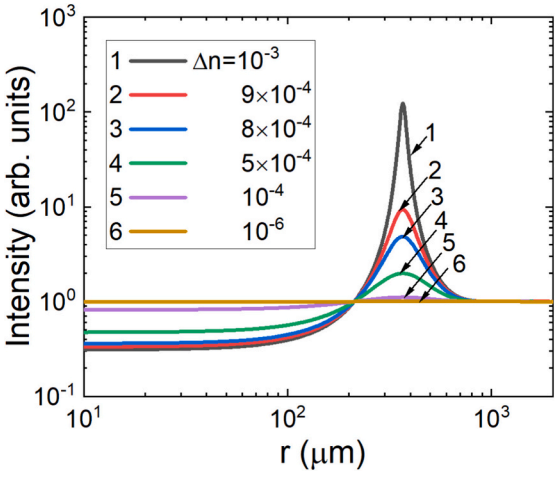


**Fig. 6.** Simulated distribution of the transmitted irradiance when an induced Gaussian refractive index profile is probed by a plane wave.

### 2.4. Impact of the two-photon absorption spatial profile

The two-photon absorption inhomogeneity determined decrease of the transmitted irradiance nearby the central range of the self-defocused beam might mimic the refraction of rays. The sample thickness integrated radial profile of the transmitted irradiance distribution $P(r,z)$, determined by the pure two-photon absorption with a coefficient $\beta$, can be simulated by using an approximated expression:

$$P(r,w,z=d) = \frac{P_0 \frac{w_0^2}{w(z)^2} \exp\left(-\frac{r^2}{w_0^2}\right)}{1 + \beta d P_0 \exp\left(-\frac{r^2}{w_0^2}\right)}. \tag{13}$$

Here, $P_0$ is the transmitted irradiance at the centre of the sample (mask) with a Gaussian profile (with inherent width $w(z)$) of the incident beam. Then, the transmitted irradiance is modified by both absorption and refraction.

The mapped profile can be approximated by the composition $S(r,w,\beta)$ of the transmitted and refracted beams at $z = L$ as

$$S(r,w,\Delta n,\beta,L) = P(r,w,d,L)\left[1 + L\frac{d\Theta(r,\Delta n,w)}{dr}\right]^{-1} \tag{14}$$

The simulated composition of transmitted irradiance $S(r,w,\Delta n,\beta,L)$ through the mask of the self-focusing beam and its components is illustrated in Fig. 7. It can be deduced from this Fig. 7 that two-photon absorption leads to blunting of the refracted beam vertex. Therefore, corrections are inevitable in order to increase the precision of the refractive index evaluation.

The two-photon absorption event actually is an inertia-less process, however, it depends on the temporal cross-correlation of the incident photon arrivals. In the case of non-degenerate ($h\nu_{G1} \neq h\nu_{G2}$) two-photon

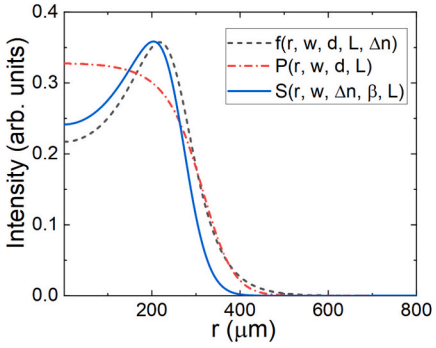


**Fig. 7.** Simulated distribution of the transmitted irradiance appears as a product $S(r,w,\Delta n,\beta,L)$ of the two-photon absorption governed transmitted irradiance $P(r,w,d,L)$ and dimension-less width of the beam $f(r,w,d,L,\Delta n)$ when an induced Gaussian refractive index and two-photon absorption profiles are probed in self-defocusing mode.

absorption of Gaussian, extremely short ($\tau_G <$ few ps) pulses, the initial phases of the transients are governed by the torsion of these pulses ($\tau_{G1} \approx \tau_{G2}$). The excess carrier $\Delta N(t,\tau_{G1},\tau_{G2},\tau_R)$ generation and recombination process is then approximated as:

$$\Delta N(t,\tau_{G1},\tau_{G2},\tau_R) \cong \frac{1}{\tau_{G2}}\int_{-\Delta t}^{\tau_{G2}} \beta \frac{P_0^2}{h\nu 1 + h\nu 2}\exp\left(-2\frac{r^2}{w^2}\right)\exp\left(-\frac{t^2}{{\tau_{G1}}^2}\right) \exp\left(-\frac{(t-\Theta)^2}{{\tau_{G2}}^2}\right)d\Theta + \Delta N(\Theta)\exp\left(-\frac{t}{\tau_R}\right) \tag{15a}$$

The torsion integral leads to the expression:

$$\Delta N(t,\tau_{G1},\tau_{G2},\tau_R) \cong \sqrt{\frac{\pi}{4}}\beta \frac{P_0^2}{h\nu 1 + h\nu 2}\exp\left(-2\frac{r^2}{w^2}\right)\exp\left(-\frac{t^2}{{\tau_{G1}}^2}\right) \left[\mathrm{erf}\left(1+\frac{t}{\tau_{G2}}\right) + \mathrm{erf}(-\Delta t)\right] + \Delta N(\Theta)\exp\left(-\frac{t}{\tau_R}\right) \tag{15b}$$

The typical shape of the transmitted irradiance temporal relaxation, modified by the simultaneous action of the refraction and two-photon absorption, has been simulated using Eq. (15) and is illustrated in Fig. 8. Measurements and analysis of the refraction-absorption transients serve for additional estimation of the prevailing mechanisms. Either beam focusing or defocusing is employed for the identification of the refractive index sign. The characteristics of decay transients and inherent components as well as their durations indicated the prevailing mechanisms in the modulation of refractive index.

It can be deduced from Fig. 8, that the amplitude of the initial component, representing cross-correlation of the Gaussian pulses, significantly prevails over the long tail governed by the recombination lifetime of the two-photon absorption-generated excess carriers. Temporal width of this initial component might serve as a benchmark of the shortest events generated by the extremely short incident pulses and the time-scale of nearly inertia-less photon interaction processes.

## 3. Instrumentation and schemes of experimental investigations

Several sets of techniques are devoted to simultaneous measurements and comprehensive analysis of $\Delta n$, $\Delta\alpha$ and two-photon ($\beta$) absorption (Pidgeon et al., 1979; Cheng et al., 2011; Catalano et al., 1988; Krauss-Kodytek et al., 2021; Eichler et al., 1986; Vaitkus et al., 1986b). The powerful techniques pointed to measurements and the separation of $\Delta n$, $\Delta\alpha$ and $\beta$ parameters comprise the $Z$-scan methodology (Said et al., 1992; Van Stryland et al., 1985; Sheik-Bahae et al., 1990; Sheik-Bahae et al., 1991a; Sheik-Bahae et al., 1991b; Sheik-Bahae et al., 1994). However, due to spectral dependent variations of the sign of the $\Delta n$ and $\Delta\alpha$ parameters, complicated variations of these characteristics

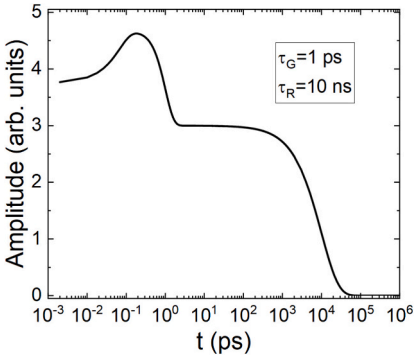


**Fig. 8.** Simulated typical transient of the transmitted irradiance is illustrated for the cross-correlated Gaussian pulses in the case of the non-degenerated two-photon absorption probed in self-defocusing mode using Eqs. 15(a) and 15(b) and parameters $\tau_G = 1$ ps and $\tau_R = 10$ ns.

dependent on excitation irradiance, as well as owing to the overlap of several mechanism impacts, measurements performed using specific optical methods (such as Z-scan) do not allow a certain and versatile examination of material and device characteristics. Transient grating techniques (Eichler et al., 1986; Vaitkus et al., 1986b) can be a powerful tool for complementary separation of the refraction mechanisms and prevailing processes. Combining optical techniques with microwave-probe-based scanners of free carrier characteristics (Gaubas et al., 2016) might efficiently supplement the reliability of material and device characterization. Also, characterization techniques based on TPA by electric current measurements had been demonstrated to control rapidly varying polarization without the need to use high-speed electronics (Kagawa, 2012). This technique had been implemented by cross-TPA measurements based on instantaneous polarization control when the two light pulses overlap. The phase difference at the position of the photodetector is measured from the TPA of the Si avalanche photodiodes, and thereby the wavelength chirping gradient can be determined. Three types of cross-TPA were well described by an analysis based on the nonlinear susceptibility tensor. The vector elements of an arbitrarily polarized signal light can be determined from the four photocurrents generated in Si-APD by cross-TPA between the signal light and the linearly polarized reference light. The time resolution of such a method is equal to the width (about 1 ps) of the employed pulses.

In this work, several optical techniques were combined and implemented using a Yb:KGW laser system (Pharos, Light Conversion) operating at a central wavelength of 1030 nm and delivering pulses with a duration of 200 fs. This system is equipped with an optical parametric amplifier (OPA) and a difference frequency generation (DFG) module (Orpheus, Light Conversion), providing the tunable output across the 210–16,000 nm spectral range.

Schematics of the experimental setups, employed for refraction-based experiments, are shown in Fig. 9. The mappings of the Gaussian beam induced refraction were implemented by using both the pump-probe (Fig. 9(a)) and self-refraction (Fig. 9(b)) regimes. In the pump-probe configuration (Fig. 9(a)), the 3 mm-thick ZnSe plane-parallel sample was excited by 200 fs pulses of a rather narrow (with a diameter of ~315 μm) Gaussian beam at 510 nm wavelength, generated by the OPA. The probe beam at the second harmonic (515 nm) wavelength of the Pharos laser has been generated in a BBO crystal. The real elements in the employed experimental setup are illustrated within the attached photo of Fig. 9(a). The temporal cross-correlation of excitation and probe pulses and synchronization for measurements of the following relaxation characteristics have been precisely controlled by varying the delay between the pump and probe pulses using a motorized optical delay line. The profile of the refraction modulated irradiance spatial distribution recorded by the probe beam, transmitted through the sample, has been mapped using a CM3-U3-13Y3M-CS 1/2″ Chameleon®3 monochrome camera. The camera gain and integration time parameters were optimized to match the dynamic range of the detected signal, keeping this response invariable throughout the measurements to ensure data comparability.

The mapping of the self-refraction spatial profiles in the nearly steady-state mode has been implemented using the scheme shown in Fig. 9(b). There, the same OPA-generated beam at 510 nm wavelength was employed. In this case, the spatial intensity distribution of the self-refracted beam was directly imaged using the CM3-U3-13Y3M-CS 1/2" Chameleon®3 camera. The camera pixel width of ~4 μm determines imaging errors. To prevent sensor saturation, appropriate density-neutral filters were placed in front of the camera entrance window. The laser beam parameters comprising incident irradiance, wavelength, and excitation beam diameter were evaluated before the mapping procedure and later maintained invariable, as in experiments on time-dependent refraction mapping. The irradiance within most of the experiments was varied over 0.2–40 GW/cm$^2$ range using delicately variable neutral optical density filters.

For the alternative measurements of $\Delta n$ variations dependent on

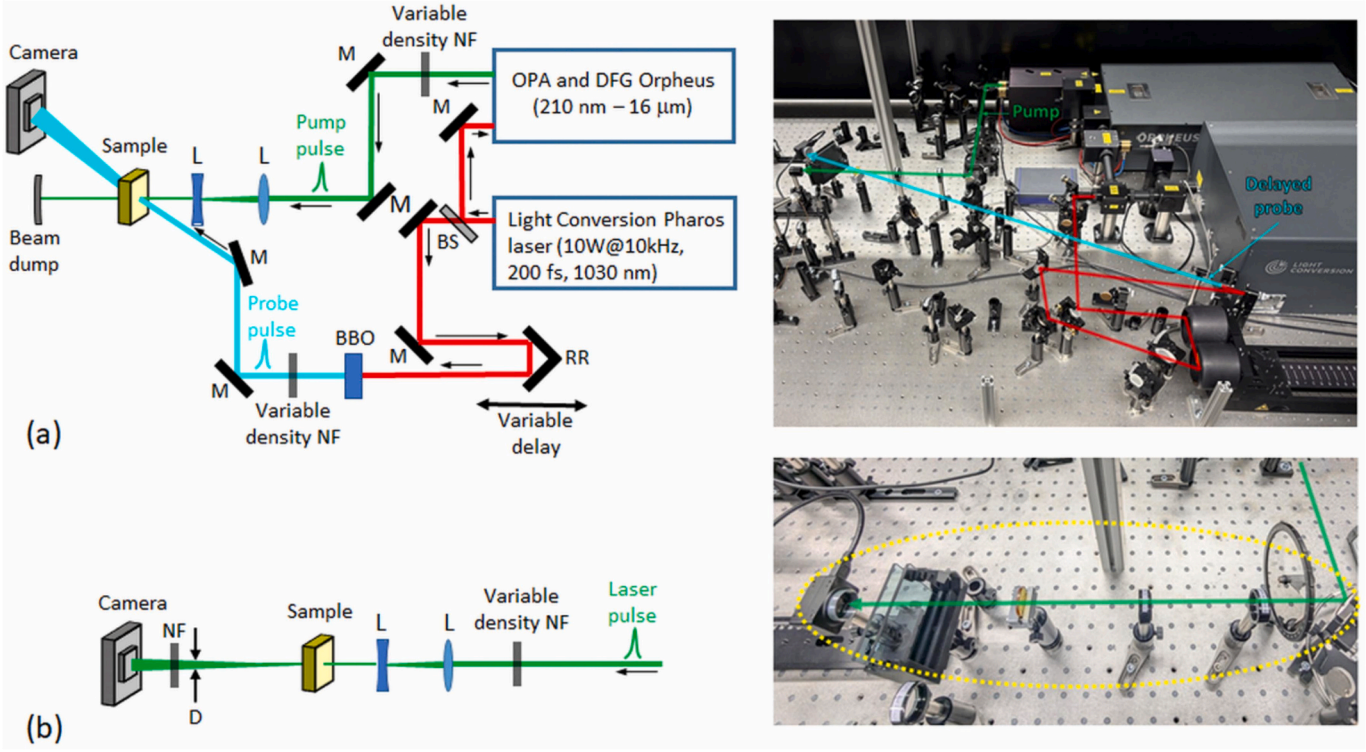


**Fig. 9.** Experimental setups and linked photos (on the right) for mapping of laser beam induced refraction in the pump-probe (a) and self-refraction (b) configurations. Here, M denotes mirror, NF is neutral filter, L is lens, BS is beam splitter, RR is a retro-reflector, BBO is a Beta-Barium Borate crystal for second-harmonic generation, and D denotes a diaphragm. The spectrally resolved beams within photos are represented by different colour lines.

irradiance, the *Z*-scan technique was employed to evaluate the sign and the magnitude of $\Delta n$ in the investigated materials (Fig. 10(a)). This method allows the evaluation of both the parameters of the refractive index as well as the nonlinear absorption characteristics. In the Z-scan configuration, the sample is translated along the beam propagation direction (z-axis) through the focal region of a focusing lens, while the transmitted power through a finite aperture (D2) in the far field is recorded as a function of sample position using the Thorlabs DET36A/M Si biased detector (Det 1 in Fig. 10(a)). The *Z*-scan setup used in this work follows the standard Z-scan configuration as described in Ref. (Sheik-Bahae et al., 1990). For the Z-scan measurements, the laser beam was spatially filtered and focused onto the sample using a lens with a focal length of $F = 100$ mm, producing a beam waist radius of approximately $w_0 = 27$ µm at the focal plane. The sample was translated along the beam propagation direction using a motorized linear translation stage over a range of ±75 mm relative to the focal position. To separate the contribution of nonlinear absorption to the refractive signal, closed-aperture *Z*-scan measurements were performed using an aperture with a transmittance of approximately 50%, positioned in the far field. The laser repetition rate was 1 kHz, and excitation wavelengths of 532 nm and 1000 nm were employed to investigate negative and positive values of $\Delta n$, respectively. Each Z-scan curve was obtained by averaging over 50 laser pulses at every sample position. The nonlinear refractive index was determined by fitting the experimental transmittance curves using the standard Z-scan formalism described in Ref. (Sheik-Bahae et al., 1990). To suppress the pulse-to-pulse laser fluctuations, a reference signal was simultaneously monitored using an identical DET36A/M detector (Det 2 in Fig. 10(a)) after splitting the incident beam.

The temporal characteristics of the free-carrier decay were examined by the technique of transient IR transmission at rather high excitation levels using the pump-probe configuration (Fig. 10(b)). Here, the pump pulse of 450 nm wavelength is used to generate the excess carriers, whereas the changes in optical absorption induced by free carriers, being proportional to the free carrier absorption (FCA) cross-section $\sigma_{eh}$ and the photo-generated carrier density $\Delta N_{eh}$, are probed by a pulse of 1030 nm wavelength light, delivered to the sample with a variable delay. The FCA induced absorption transient is monitored through measurements of the probe beam differential absorption (DA) signal:

$$DA(t) = ln\frac{I_{unexc}}{I_{exc}(t)} = \Delta N_{eh}\sigma_{eh}d \bullet \exp\left(-\frac{t}{\tau_{DA}}\right) \tag{16}$$

Here, $I_{unexc}$ and $I_{exc}(t)$ represent the intensities of the probe beam passing through the sample without and with a pump pulse, respectively, $d$ is the sample thickness, and $\tau_{DA}$ is the free-carrier decay time, inherent for the transmission measurements at high density excitations. The diameter of the probe beam has been chosen to be at least 3 times smaller than that of the pump beam.

The MW-probed photoconductivity transients have been synchronously recorded by a real-time 2 GHz LeCroy oscilloscope using the setup, shown in Fig. 10(c). These measurements were addressed to verify the simultaneous excitation of the excess carriers introduced through the TPA absorption processes and to record their recombination time at relatively low excitation levels.

The irradiance $P_0$ for all the experimental setups was evaluated using widely accepted approach, employing the measured average laser power, beam area, pulse repetition rate, and pulse duration. The average power $P_{av}$ of the laser radiation was measured using an Ophir Nova II power meter equipped with an Ophir PD300-UV sensor. The beam area $S$ was determined from the recorded beam profiles using a CM3-U3-13Y3M-CS 1/2″ Chameleon®3 camera and confirmed using the knife-edge technique. For the laser repetition rate $f = 1$ kHz and the pulse duration $\tau_{pl} = 200$ fs, the peak irradiance has been evaluated as

$$P_0 = \frac{P_{av}}{f \bullet \tau_{pl} \bullet S}. \tag{17}$$

The commercial ZnSe plane-parallel surface-polished 2–3 mm thick optical windows have been chosen as a material for the research of

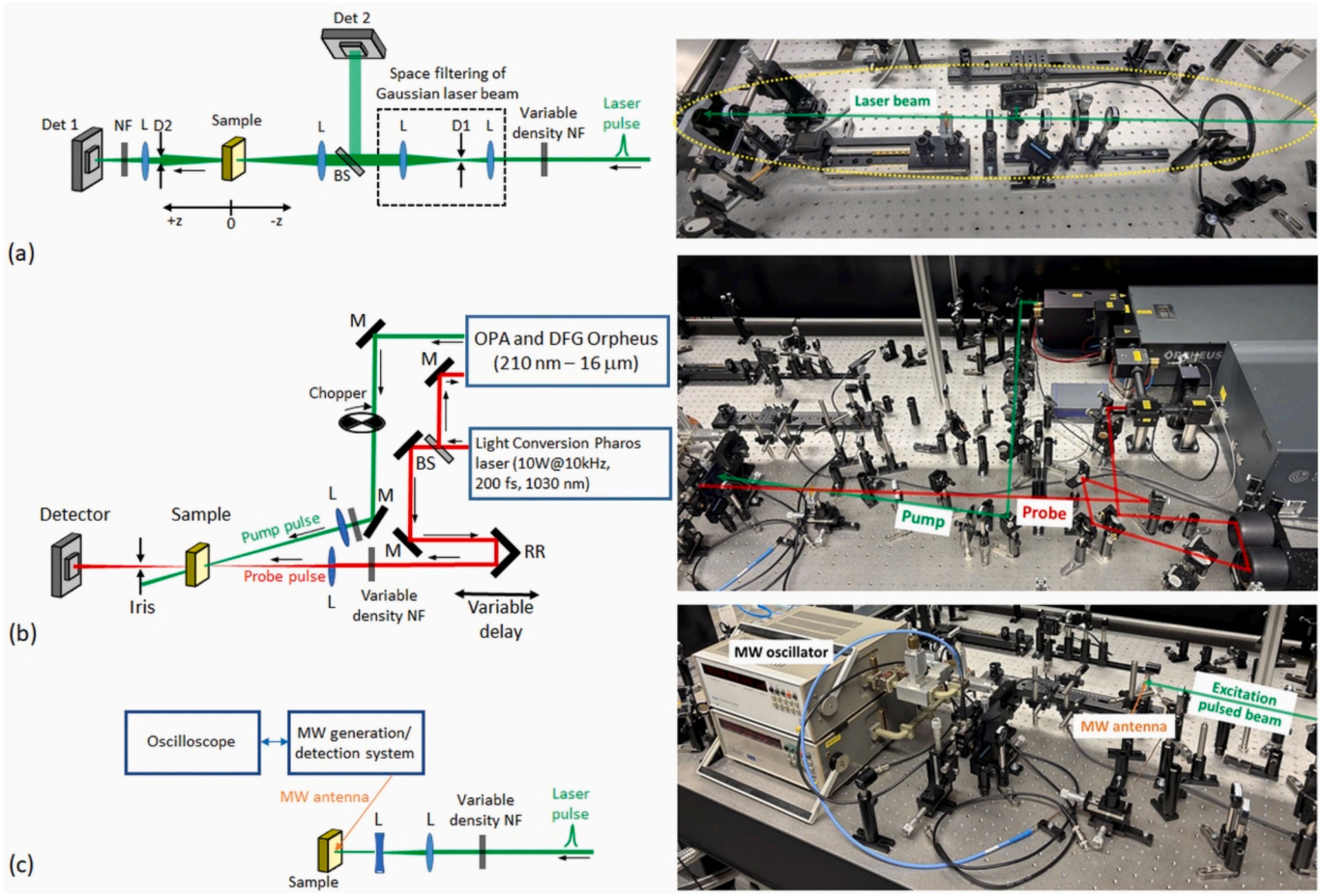


**Fig. 10.** Experimental setups and linked photos (on the right) employed for the implementation of *Z*-scan (a), transient IR absorption in the pump-probe configuration (b) and microwave-probed excess carrier decay transient measurements (c). Here, the abbreviations denote as follows: M mirror, NF neutral filter, L lens, BS beam splitter, RR a retro-reflector, D a diaphragm, Det 1 and Det 2 the identical Si detectors used for monitoring of the transmitted signal as well as the reference beam (reflected from the beam splitter) to suppress the impact of the laser intensity fluctuations, respectively. The transient MW probed photoconductivity technique (c) has been applied to synchronously verify the induced excess carrier concentration and to control their relaxation together with the TPA absorption process. Far from the focus, the irradiance is low, and nonlinear effects during *Z*-scan procedure are negligible. As the sample approaches the focal plane, the increased irradiance induces self-focusing or self-defocusing, resulting in a narrowing or broadening of the transmitted beam at the aperture, depending on the sign of the nonlinear refractive index. As the sample passes through the focus, the reverse behaviour of beam parameters appears, producing the characteristic *Z*-scan transmittance curve. Here, the spectrally resolved beams within photos are also represented by different colour lines.

refraction characteristics. ZnSe is a direct-bandgap semiconductor ($E_g \approx$ 2.7 eV) with a wide optical transparency range extending from the visible to the infrared spectral region, making it highly suitable for nonlinear optical studies over a broad range of excitation wavelengths. The ZnSe material was chosen because most of its parameters are well established, including a picosecond excitation range, where the contributions of two-photon absorption, free-carrier generation, and carrier-induced refractive-index changes had been distinguished. High-quality commercial ZnSe optical windows with excellent surface polishing and low scattering losses are readily available, which improves reproducibility and minimizes distortions associated with material inhomogeneity or surface imperfections. This provides a reliable reference framework for validating the developed models and experimental techniques, as well as a benchmark for comparison of the experimentally extracted nonlinear refraction parameters obtained in the present work.

## 4. Results of the mapping of the refractive index modulation dependent on irradiance using various regimes

### 4.1. Parameters of the employed beams and material under tests

The irradiance-dependent modulation of the refractive index is highly sensitive to the parameters of the incident laser beam. In this work, the rather narrow Gaussian beams generated by a femtosecond laser system have been exploited. The beam spread and the corresponding irradiance variation as a function of the propagation distance $L$ between the beam output plane and the mapping camera are technical prerequisites, critical for accurate mapping of the refracted beam intensity distribution and for the subsequent analysis of the experimental results.

To evaluate these characteristics, the spatial beam spread during free-space propagation was measured as a function of distance $L$ of the position between the sample output plane and the camera. The evaluated beam width is then routinely used to estimate the local irradiance at different propagation distances. The recorded characteristics are shown in Fig. 11. The radial ($r$) and distance ($L$) dependent irradiance distribution of the Gaussian beam can be approximated by

$$P(r,L) = P_0\left(\frac{w_0}{w(L)}\right)^2 exp\left(-\frac{r^2}{w(L)}\right)^2, \tag{18a}$$

where $P_0$ is the peak irradiance at the beam waist, $r$ is the radial coordinate, and the probe beam radius $w(L)$ evolves with propagation distance according to

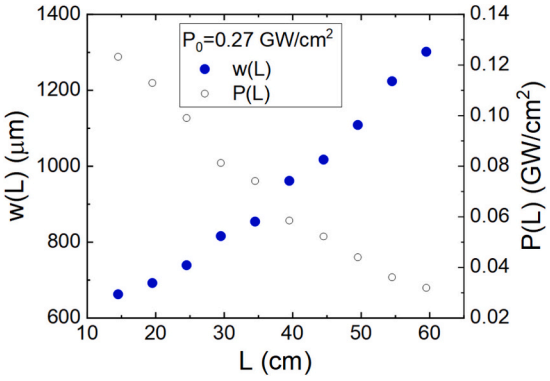


**Fig. 11.** Spread and irradiance variations dependent on the distance $L$ between the sample (serving as a mask with an introduced refractive index profile) position and the camera exploited for refracted beam mapping.

$$w(L) = w_0\left(1 + \left(\frac{L\lambda}{\pi w_0^2}\right)^2\right)^{1/2}. \tag{18b}$$

The refractive index modulation is specifically dependent on the local irradiance. However, different physical mechanisms govern modifications in refractive characteristics at different irradiance levels. At relatively low excitation levels, the nonlinear refraction is primarily governed by third-order optical non-linearities. As the irradiance increases, the higher-order nonlinear effects become significant in the tail segments of relaxation process. In particular, an effective fifth-order nonlinearity may arise from the generation of excess carriers via two-photon absorption (TPA), which subsequently modifies the refractive index changes. In the present experiments, the generation of free carriers at elevated values of irradiance becomes unavoidable. To confirm carrier excitation and to monitor the relaxation dynamics of the photo-generated carriers, microwave probed photoconductivity (MW-PC) transients were simultaneously recorded. A typical MW-PC transient recorded on the ZnSe sample under band-to-band excitation is shown in Fig. 12. From these measurements, the effective carrier recombination lifetime $\tau_R$ of 30 ns has been estimated.

### 4.2. Imaging of refracted beams

Imaging of the refracted beams was performed in two different configurations: (i) the self-refraction regime, in which Gaussian-shaped refractive index profiles are synchronously mapped in the quasi-steady-state regime, and (ii) the probe beam refraction configuration (using pump-probe regime), in which a rather weak intensity, enlarged-diameter probe beam is used to map the laser-induced refractive index profile without significantly perturbing it. In the latter case, the probe beam is close to the plane wave, enabling direct mapping of refractive index gradients.

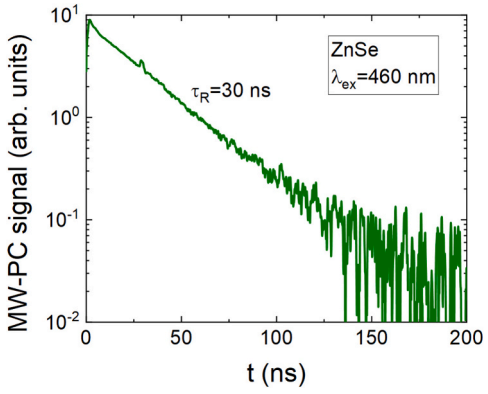


**Fig. 12.** Decay of excess carrier concentration recorded by microwave probed photoconductivity technique simultaneously with refracted beam mapping implemented using pump-probe regime. The estimated recombination lifetime is $\tau_R = 30$ ns.

The evolution of the cross-sectional self-refraction beam profiles, mapped at a distance of $L = 14.5$ cm from ZnSe sample, is illustrated in Fig. 13(a) for the peak irradiances $P_0$ varied in the range from 0.3 to 27.6 GW/cm$^2$. At 0.3 GW/cm$^2$, no noticeable deviation from the initial Gaussian beam shape is observed. This determines the self-refraction mapping limit (of $P_0 \leq 0.3$ GW/cm$^2$) relative to the incident irradiance. As the irradiance increases to $P_0 \geq 0.6$ GW/cm$^2$, the beam profile begins to deviate from the Gaussian shape, with the central region flattening and increase of the beam width. At $P_0 = 2.0$ GW/cm$^2$, the intensity distribution approaches an almost flat-top shape. For the further elevated values of irradiance, namely $P_0 \geq 3.2$ GW/cm$^2$, a clear ring-shaped intensity distribution emerges. This effect becomes increasingly prominent due to strong modulation of the refractive index $\Delta n$, which results in the enhanced defocusing of the laser beam. The two-dimensional intensity map of the self-refracted beam recorded at $P_0 =$ 27.6 GW/cm$^2$ clearly confirms the formation of a well-defined ring-shaped profile.

The pump-probe regime has been implemented using pulses of the narrow pump (with beam waist of $w_0 = 160\,\mu$m) beam at $\lambda = 510$ nm wavelength and flat wave probe. The probe beam with waist ($w_0 > 1000$ μm) was significantly wider than the pump one, which was also separated in wavelength. The probe wavelength of $\lambda = 515$ nm was chosen to distinguish the pump and probe constituents. In spectral refraction mappings, the probe irradiance was maintained several orders of magnitude below that of the pump beam to prevent any probe-induced modification of $\Delta n$. Temporal overlap of the pump and probe pulses has been achieved using a computer-controlled optical delay line. The two-dimensional probe intensity map and the corresponding perpendicular cross-sectional profiles of the refracted probe are illustrated in Fig. 14. The observed ring-shaped structure provides clear evidence that the probe beam is defocused by the pump-pulse-generated refractive index gradients. On the other hand, the appearance of the structured light for the elevated irradiance involved in the technique of the probe beam mapping clearly demonstrates the opportunity of lens-less profile manipulations of the refracted beams for laser technology purposes.

### 4.3. Exclusion of the impact of the two-photon absorption in the refracted beam profiling

At the typical irradiance levels employed in the present experiments, the nonlinear two-photon absorption (TPA) becomes significant. Consequently, the spread beam profiles are influenced not only by refraction, but also by intensity-dependent nonlinear absorption, particularly in regions of elevated irradiance.

To accurately isolate the contribution of beam refraction from that of nonlinear absorption, the experimentally measured intensity distribution profiles have been corrected excluding TPA from the refraction profiles. This correction procedure is illustrated in Fig. 15 using a few refraction images obtained at different irradiance values. There, the experimentally recorded intensity distribution profile (black dotted curve in Fig. 15) represents the combined impact of the refraction and two-photon absorption. The correction factor accounting for TPA, denoted as $C_{TPA}(r)$ (red dashed curve in Fig. 15), is expressed as

$$C_{TPA}(r) = 1 + \beta P_0 exp\left(-\left(\frac{r}{2w_0}\right)^2\right)d, \tag{19}$$

where $\beta$ is the two-photon absorption coefficient, $P_0$ is the peak irradiance, and $w_0$ is the Gaussian beam waist radius. The influence of two-photon absorption is removed by multiplying the experimentally measured intensity distribution $I_{exp}(r)$ by the correction factor $C_{TPA}(r)$.

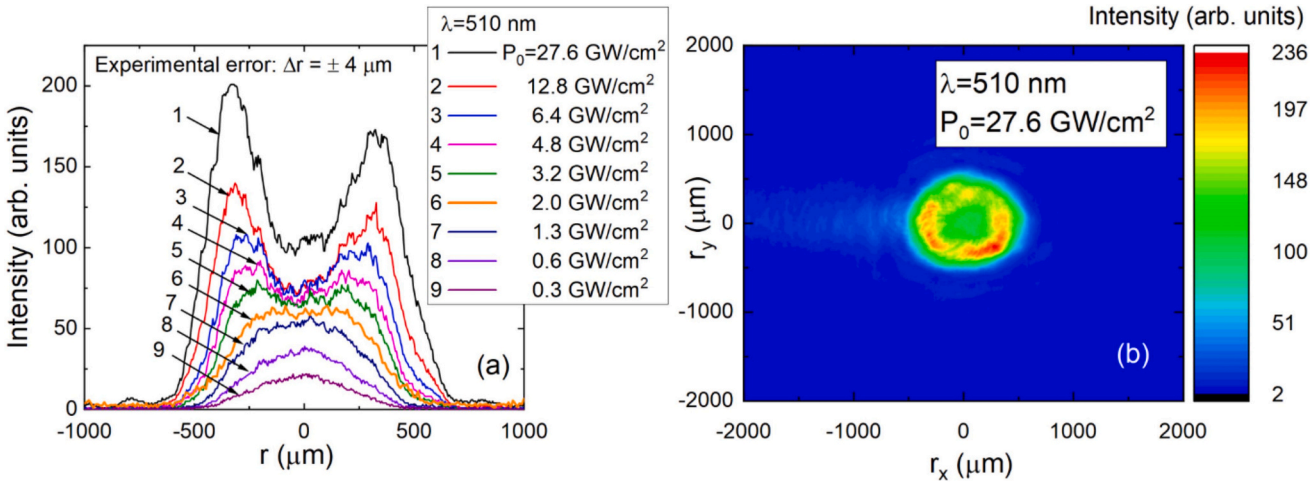


**Fig. 13.** (a) Mapped evolution of the cross-sectional distribution of transmitted irradiance in self-refracted beams at $\lambda = 510$ nm wavelength as a function of irradiance. The mapping precision is determined by camera pixel parameter of 4 μm width. (b) The map of the recorded radial distribution locating the camera at $L = 14.5$ cm from the ZnSe plate, corresponding to a rather rigour optics ray Fresnel distance regime. The experimental error in the measurement of the radial coordinate of beam mapping comprises $\Delta r = \pm 4$ μm.

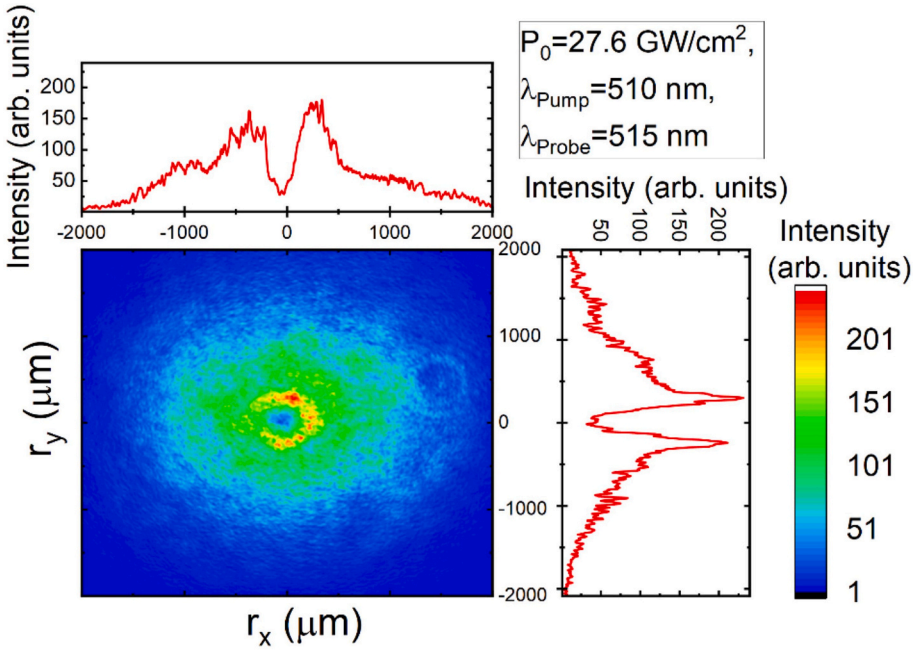


**Fig. 14.** The lateral refracted irradiance distribution profiles observed by mapping probe beam at fixed irradiance of the pump pulse. The distance between the sample and the camera has been fixed at $L = 14.5$ cm.

This procedure yields the reconstructed intensity profile, shown as the green solid curves in Fig. 15. The reconstructed profiles are subsequently simulated (blue dash-dotted curves in Fig. 15) using the theoretical approach of the TPA-governed beam profile changes. These procedures enable more reliable extraction of the absolute values of the refractive index modulation $\Delta n$. At the elevated irradiance values (Fig. 15(a) and (b)), the results clearly demonstrate that non-linear absorption plays a substantial role and must be accounted for in any quantitative analysis of the refractive index modulation. While, the reconstructed intensity distributions indicate that at low irradiance (Fig. 15(c)), the contribution of the non-linear two-photon absorption is nearly negligible.

### *4.4. Characteristics of self-refraction profiles dependent on the distance of the mapping camera and irradiance*

The irradiance-dependent refractive index modulation $\Delta n$ has been comprehensively evaluated by fitting experimentally measured self-refraction intensity profiles to numerically simulated ones. The simulations were performed using the following expression for the refracted beam intensity distribution:

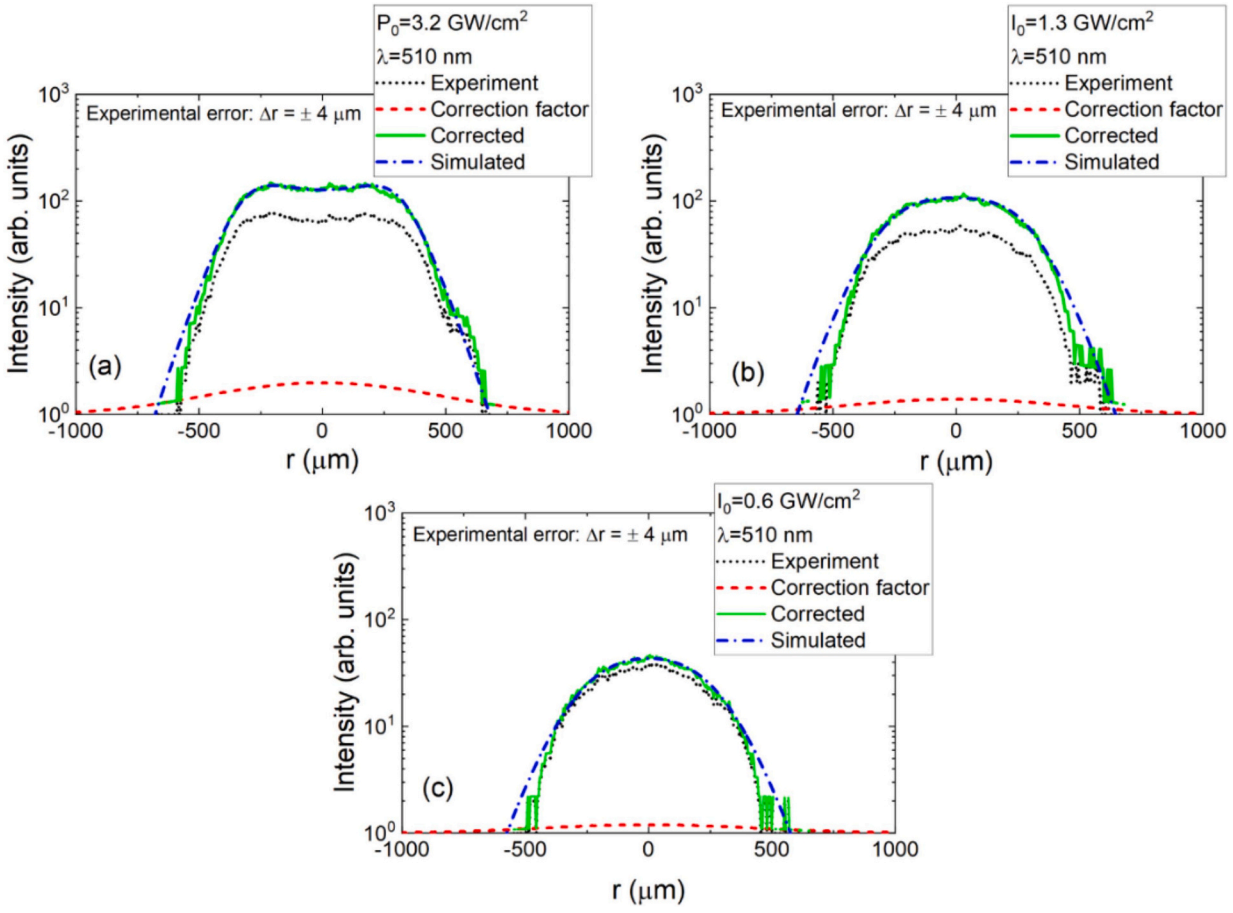


**Fig. 15.** Illustration of the reconstruction and fitting of the experimental self-refraction intensity distribution profiles modified due to non-linear two-photon absorption (TPA) at different irradiances: (a) $P_0 = 3.2$ GWcm$^2$, (b) $P_0 = 1.3$ GWcm$^2$ and (c) $P_0 = 0.6$ GWcm$^2$. The black-dotted curves represent the experimentally recorded intensity distribution profiles of the transmitted beam, containing contributions from both nonlinear refraction and TPA. The red-dashed curves show the calculated TPA correction factor $C_{TPA}(r)$. The green solid curves represent the reconstructed beam profiles as $I_{exp}(r)\cdot C_{TPA}(r)$ corrected for nonlinear absorption effects. The blue dash-dotted curves show the simulated refraction profiles calculated using Eqs. (20a) and (20b), fitted to the reconstructed experimental profiles for the extraction of the refractive index modulation $\Delta n$. The intensity profiles represent the experimentally measured scale without additional normalization. (For interpretation of the references to colour in this figure legend, the reader is referred to the web version of this article.)

$$I(r,\Delta n,L) = I_0(r,L) \bullet \left( \left( 1 + \frac{2Ld}{(w(L))^2} \bullet \frac{\left( \frac{n_0}{\Delta n} \bullet exp\left( \frac{r^2}{(w(L))^2} \right) \bullet \left( 1 - 2\frac{r^2}{(w(L))^2} \right) - 1 \right)}{\left( \frac{n_0}{\Delta n} \bullet exp\left( \frac{r^2}{(w(L))^2} \right) - 1 \right)^2} \right)^{-1} \right), \tag{20a}$$

where the initial intensity distribution of the probe beam is given as

$$I_0(r,L) = P_0 \bullet exp\left( \frac{-r^2}{(w(L))^2} \right) \bullet \frac{w_0^2}{(w(L))^2} \tag{20b}$$

Here, $I_0(r,L)$ describes the Gaussian intensity profile of the incident beam and its evolution with propagation distance $L$ between the position of the sample exit plane and the mapping camera. In the fitting procedure, the independently measured experimental parameters, including the beam waste radius $w_0$, propagation distance $L$, sample thickness $d$, incident irradiance $P_0$, and excitation wavelength $\lambda$, have been fixed. The refractive index modulation $\Delta n$ was used as the only adjustable fitting parameter. Each experimental profile was obtained by integrating the signal over several milliseconds, thereby collecting several profiles at a laser repetition rate of 1 kHz. No background correction, nor additional smoothing procedure was applied. The fitting was performed over the radial range where intensity levels exceeded 5% of the peak intensity to avoid the influence of detector noise at the beam periphery. The optimal value of $\Delta n$ was determined by minimizing the

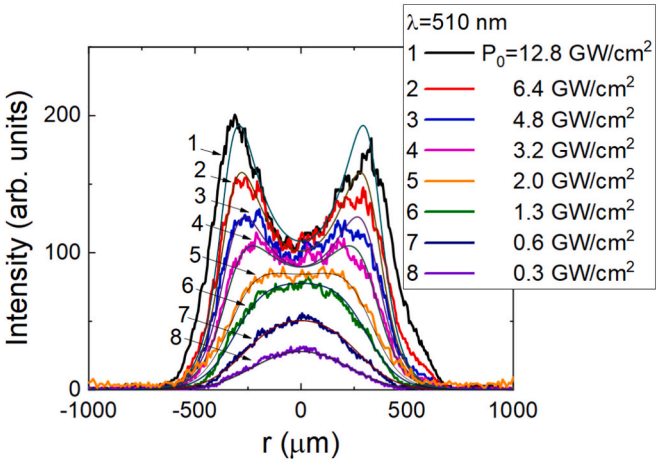


**Fig. 16.** Comparison of experimentally measured and simulated radial intensity distribution profiles of self-refracted laser beams for incident irradiances ranging from 0.3 to 12.8 GW/cm$^2$.

least-squares deviation employed for control of the experimental and simulated profile fitting procedure. The uncertainty of the extracted $\Delta n$ values was estimated from repeated measurements, yielding an estimated relative uncertainty of approximately $\leq$10%.

The thick noisy curves represent the experimentally recorded intensity profiles of the transmitted beam, while the thin solid curves correspond to profiles simulated using Eqs. (20a) and (20b). The simulated profiles were fitted to the experimental data by varying the refractive index modulation $\Delta n$, while the experimentally measured beam parameters and propagation distance were kept fixed. The comparison illustrates the irradiance-dependent transformation of the beam profile from a Gaussian-like to a ring-shaped distribution and the quality of the fitting procedure used for the extraction of $\Delta n$. The experimental error in the measurement of the radial coordinate in beam mapping comprises $\Delta r = \pm 4$ μm.

Fig. 16 illustrates the fitted evolution of the experimentally obtained cross-sectional intensity profiles of the self-refracted beams as a function of incident irradiance, together with the respective fitting profiles, simulated using Eqs. (20a) and (20b). The simulated profiles show a good agreement with the experimental data over the entire irradiance range investigated, confirming the validity of the applied fitting procedure.

The laser beam intensity profile, modified by refraction due to irradiance-induced refractive index modulation $\Delta n$, caused by probe beam broadening and two-photon absorption, also evolves with the propagation distance $L$ between the exit plane of the ZnSe sample and the mapping camera. A comparison of the experimentally measured and simulated intensity distribution profiles as a function of $L$ is shown in Fig. 17(a) and Fig. 17(b), respectively. The experimental and simulated profiles exhibit good qualitative agreement over the investigated propagation distances. With increasing $L$, a gradual decrease in the peak intensity is observed, accompanied by an expansion of the ring diameter formed by refraction-induced beam reshaping. These trends arise primarily from Gaussian beam parameter variations during free-space propagation and divergence of the incident beam, which governs the evolution of the beam waist and irradiance with distance. Consequently, the distance-dependent beam spreading also plays a key role in determining the observed self-refraction patterns and the spatial characteristics of the refractive index modulation.

The simulation based refractive index values have been extracted, to plot the characteristic being a function of irradiance and to compare with those measured using different methods in ZnSe material.

### 4.5. Results of the pump-probe refraction shaping regime correlated with MW-PC transients

Mapping of the laser-induced Gaussian refractive index profile using a quasi-plane-wave probe was performed in a pump-probe configuration employing the experimental setup shown in Fig. 9(a). The ZnSe sample has been illuminated with a rather narrow Gaussian pump beam with a waist radius of $w_0 \approx 160$ μm at a wavelength of 510 nm. The induced refractive index modulation was probed using a low-intensity and significantly wider Gaussian beam with a waist of $w_0 \geq 1$ mm at a wavelength of 515 nm. The two-directional intensity distribution maps recorded by using the probe beam with and without of the pump pulse are illustrated in Fig. 18. The normalized intensity map of the transmitted probe beam recorded under pump irradiation with a peak irradiance of $P_{pump} = 27.6$ GW/cm$^2$ is shown in Fig. 18 (a). In the absence of pump (Fig. 18(b)), the probe beam intensity distribution is almost radially uniform over radial coordinate changes when compared to the pump beam diameter. This illustrates an opportunity to probe the refractive index lateral distribution using the plane-wave. The normalization of the transmitted irradiation was performed with respect to that of the probe beam, i.e. represented as $(I_{\text{probe}}(P_{\text{pump}} = 27.6\ \text{GW/cm}^2))/(I_{\text{probe}}(P_{\text{pump}} = 0))$. This representation emphasizes the pump-induced beam reshaping and clearly reveals the formation of a ring-shaped distribution in beam structuring for the probe. For comparison, the cross-sectional profiles of the probe beam recorded with and without the pump pulse are shown in Fig. 19(a).

The refracted beam profiles obtained using the self-refraction and pump-probe refraction regimes under identical pump beam parameters are compared in Fig. 19(b). The close correspondence between the characteristic features of both profiles provides further confirmation of laser-induced refractive index modulation and its decisive role in shaping of probe beams. These illustrations directly demonstrate the irradiance-controlled opportunity of the lens-less temporal manipulations of refraction-structured light beams for laser technology purposes.

The normalized probe beam radial irradiance distribution profiles obtained at different pump irradiance values are illustrated in Fig. 20. The normalized values below unity at the beam centre indicate a reduction of the transmitted irradiance, whereas values exceeding unity correspond to the enhanced intensity in the outer regions due to refraction induced structuring of the probe beam, confirming the formation of ring-shaped profiles and the opportunity to govern the probe beam intensity and profile varying pump irradiance. There, the irradiance at the beam centre decreases while the intensity of the outer ring

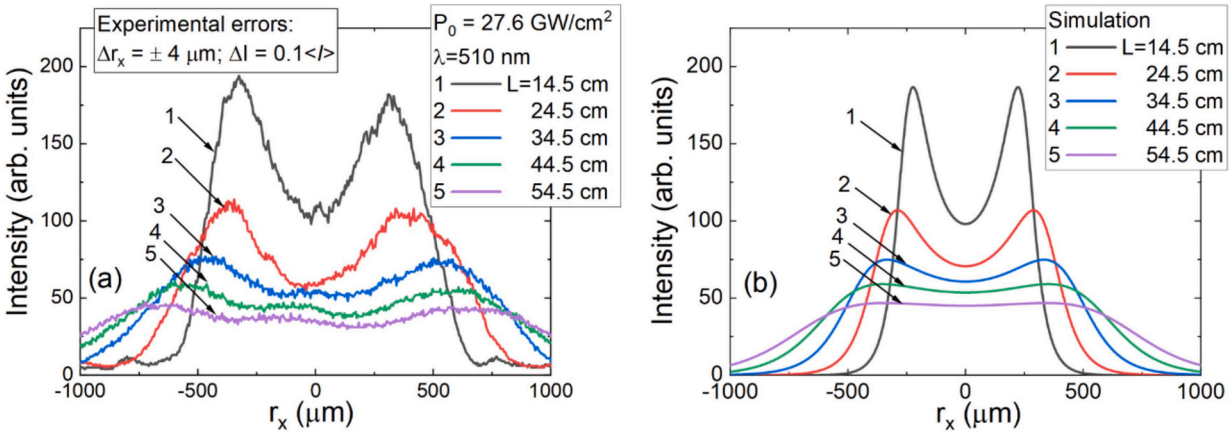


**Fig. 17.** Evolution of the cross-sectional intensity distribution profiles of self-refracted laser beams as a function of the propagation distance $L$ between the ZnSe sample exit plane and the mapping camera at fixed incident irradiance: (a) experimentally measured profiles and (b) profiles simulated using Eqs. (20a) and (20b). The profiles, obtained in experiments, represent the measured transverse intensity distributions of the transmitted beam, while the simulated profiles were calculated using the extracted refractive index modulation $\Delta n$ and independently measured beam parameters. The comparison illustrates the evolution of beam broadening and ring-shaped profile formation during free-space propagation and shows the agreement between experimentally mapped and theoretically reconstructed beam-shaping characteristics.

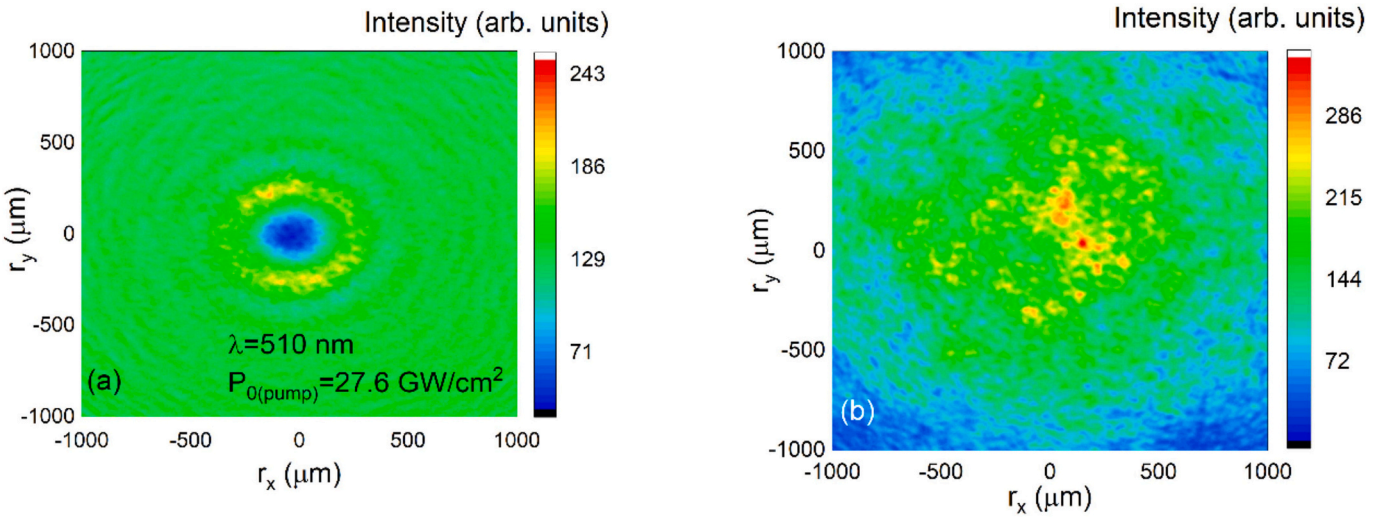


**Fig. 18.** Lateral irradiance beam distribution profiles ascribed to the probe beam recorded in the pump-probe refraction configuration: (a) normalized probe-beam intensity distribution measured in the presence of the pump pulse at $P_{pump} = 27.6$ GW/cm$^2$, and (b) probe beam intensity distribution recorded in the absence of the pump pulse $P_{pump} = 0$. The intensity map in (a) is presented as the ratio $I_{\text{probe}}(P_{\text{pump}} = 27.6\ \text{GW/cm}^2))/(I_{\text{probe}}(P_{\text{pump}} = 0)$ in order to highlight the pump-induced refraction caused probe beam structuring and the formation of the ring-shaped profile.

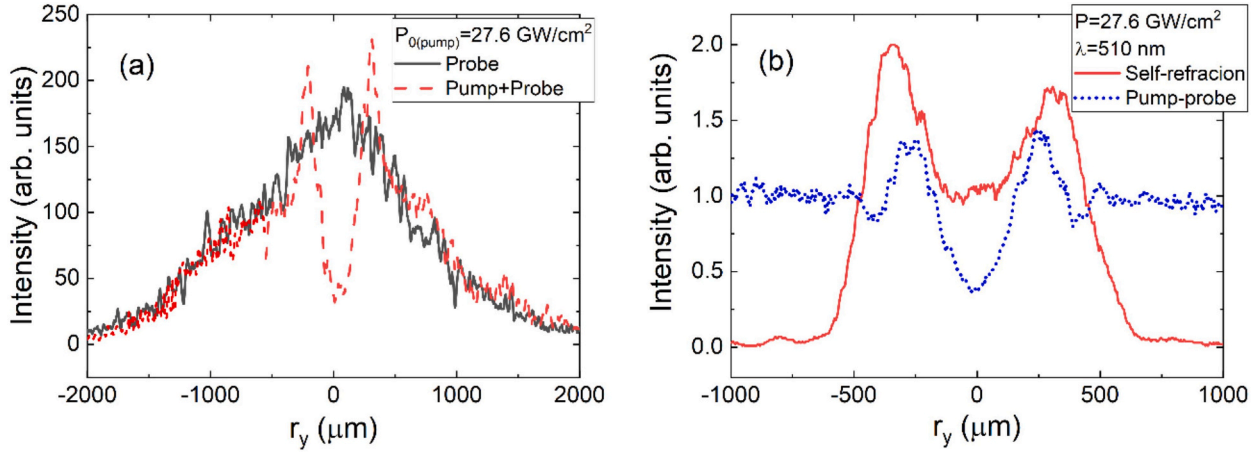


**Fig. 19.** (a) Profiles for the cross-sectional transmitted irradiance distribution mapped in vicinity of the centre of the probe beam in the presence ($I_{\text{probe}}(P_{\text{pump}} = 27.6$ GWcm$^2$)) and absence ($I_{\text{probe}}(P_{\text{ump}} = 0)$) of the pump beam. (b) Comparison of the radial irradiance distribution profiles obtained in the self-refraction and pump-probe regimes under identical pump irradiance conditions. The Gaussian beam-induced refraction profile is presented as the normalized ratio $I_{\text{probe}}(P_{\text{pump}} = 27.6$ GWcm$^2$)$/I_{\text{probe}}(P_{\text{pump}} = 0)$ in order to highlight the pump-induced refractive redistribution of the probe beam. The self-refraction profile is vertically scaled to a value of 2 for clarity of visual comparison. The comparison demonstrates the similarity of the beam reshaping behaviour obtained using direct self-refraction and externally probed refractive index mapping in ZnSe sample.

increases with enhancement of the pump irradiance. This indicates an enhancement of the refractive index modulation $\Delta n$.

The experimental probe beam profiles were fitted employing simulated profiles obtained using Eqs. (20a) and (20b). The simulations show good agreement with the experimental data over the investigated irradiance range.

### 4.6. Cross-correlational and temporal variations of the pump-probe beams

The temporal evolution of pump-induced refraction characteristics of the ZnSe sample has been examined using a pump-probe configuration and incorporating a computer-controlled optical delay line. Differential absorption (DA) decay transients associated with free-carrier absorption (FCA) were measured using the experimental setup presented in Fig. 10(b). A recorded FCA transient obtained is illustrated in Fig. 21(a). Free carriers were generated via band-to-band excitation using wavelength of $\lambda_{ex} = 450$ nm, while the transient of the differential absorption was probed by delayed 1030 nm pulses. This FCA transient contains a fast initial component on a few picosecond time-scale (Fig. 21 (a)), followed by a slower asymptotic decay with a characteristic time-scale of nanoseconds. The ultrafast component originates from the temporal cross-correlation of the overlapping 200 fs pump and probe pulses, whereas the slower component is attributed to free-carrier recombination.

To further resolve the temporal contribution of two-photon absorption, differential absorption (DA) scanned by the probe beam pulse was also recorded at 1030 nm pump. Here, photon energy of 1.2 eV, has been selected below $E_g/2$ of ZnSe in order to avoid pump-induced two-photon absorption. While, the probe at 830 nm (with photon energy 1.5 eV, being above $E_g/2$) was employed. The sufficiently lower intensity of this probe was applied in order to exclude the probe-induced two-photon absorption. The DA transient, recorded at above discussed conditions, is shown in Fig. 21(a) by blue curve, denoted as DA. Owing to the instantaneous (inert-less) nature of the two-photon absorption process,

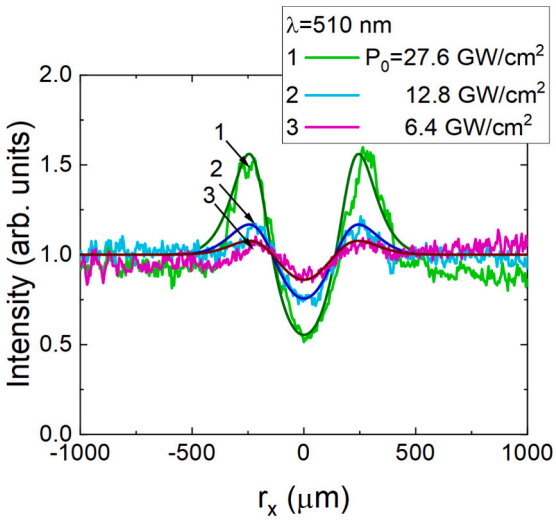


**Fig. 20.** Evolution of the radial irradiance distribution profiles modified by the pump-induced refraction and recorded using different pump pulse irradiances. The thick noisy curves represent the experimentally recorded profiles, while the thin solid curves correspond to profiles simulated using Eqs. (20a) and (20b). The experimentally measured refraction profiles are presented as the normalized ratio $I_{probe}(P_{pump})/I_{probe}(P_{pump} = 0)$, where $I_{probe}(P_{pump} = 0)$ is the probe beam intensity distribution recorded in the absence of the pump pulse. Values below unity at the beam centre indicate pump-induced intensity reduction due to self-defocusing, whereas values above unity correspond to intensity enhancement in the outer regions associated with ring-shaped beam formation ascribed to the probe beam. The simulated profiles were fitted to the experimental data by varying the refractive index modulation $\Delta n$, illustrating the irradiance-dependent evolution of the induced refractive index distribution.

the DA signal is confined to time interval of $\delta\tau < 1$ ps, determined by the cross-correlation of the two overlapping 200 fs laser pulses.

Fig. 21(b) illustrates the temporal evolution of the radial (RM) refracted irradiance distribution profiles mapped by the probe beam under varied pump irradiance. A complete set of temporal evolution of the RM profiles employed to restore the RM transient is presented in Fig. 21(c). The irradiance variation in the central region of the refracted probe beam is quantified by plotting the inverted signal, rescaled by a function $dI = -(1 - I)$, which is overlaid with the DA and FCA transients in Fig. 21(a). A clear correlation is observed between the temporal evolution of this inverted probe intensity and the FCA decay transient. In the initial segment of the temporal overlap region within a transient (Fig. 21(a)), the inverted probe intensity increases due to cross-correlation of the pump-probe pulses. This behaviour is associated with non-degenerate two-photon absorption, which occurs when the pump and probe pulses start to overlap in time and reaches a maximum at complete temporal overlap. Simultaneously, the formation of a ring-shaped irradiance distribution profile, ascribed to the probe beam, is observed (Fig. 21(b) and (c)). As the pump and probe pulses become separated temporally, the inverted signal amplitude ascribed to probe beam decreases, and the ring-shaped profile disappears. At longer delay times, a secondary formation of the ring-shaped intensity profile is observed, which is attributed to probe-beam refraction induced by the pump-generated refractive index modulation. This ring-shaped structure gradually diminishes with increasing delay, in direct correlation with the decay of the DA and FCA transients (Fig. 21(a)), indicating relaxation of the concentration of free-carriers and the corresponding decline in the refractive index modulation $\Delta n$. The agreement between the relaxation time-dependent weakening of the refraction signal within RM and the FCA transients provides evidence that free carriers impact the nonlinear refractive response variations. The pump-probe measurements reveal two distinct temporal regimes contributing to the observed probe-beam reshaping. The ultrafast signal observed within the cross-correlated pump and probe pulses ($\delta\tau < 1$ ps) predominantly originates from nondegenerate two-photon absorption and represents a cross-correlation effect associated with the simultaneous interaction of the overlapping femtosecond pulses. This contribution is instantaneous and disappears as the pulses become temporally separated. In contrast, the refractive beam reshaping and differential absorption components, persisting at longer delay times, correlate with the decay of the MW-PC and FCA transients, indicating that these slower processes are governed by photo-generated free carriers. A rough estimate of the generated carrier density was performed assuming carrier generation via two-photon absorption under the employed excitation conditions. Using the experimentally applied irradiance range and the reported two-photon absorption $\beta = 5.8$ cm/GW (Sheik-Bahae et al., 1990) for ZnSe, the excess carrier density was estimated to be on the order of $10^{16}$–$10^{18}$cm$^{-3}$. Such carrier densities are sufficient to produce a measurable negative refractive-index contribution through the free-carrier plasma response described by the Drude model (Dresselhaus et al., 2018). Therefore, the experimentally observed negative sign of $\Delta n$ and the accompanying beam self-defocusing behaviour are consistent with carrier-induced refractive index modulation. This is an advantage of the refracted beam mapping technique, which enables simultaneous and direct evaluation of refractive index sign and value by avoiding tedious profiling of the differential integral *Z*-scans, and which introduces additional uncertainties due to variations of the beam parameters ($w_0$, $P_0$, *etc*) and structuring of light.

### *4.7. Beam area integrated refractive index characteristics evaluated using the Z-scan technique.*

Irrespective of some shortcomings of the Z-scan technique, the irradiance-dependent refractive index variations induced by laser excitation were alternatively and independently verified using the well-established *Z*-scan technique (Said et al., 1992; Van Stryland et al., 1985; Sheik-Bahae et al., 1990; Sheik-Bahae et al., 1991a; Sheik-Bahae et al., 1994). The experimental Z-scan setup employed in this work is presented in Fig. 10(a). The Z-scan recorded differential refraction curves obtained for 3 mm thick ZnSe optical windows are shown in Fig. 22. There, the *Z*-scan differential profiles obtained for the cases of negative and positive refractive index quantities are illustrated in figures (Fig. 22(a)) and (Fig. 22(b)), respectively. The measurement results shown in Fig. 22 were obtained using excitation wavelengths of 532 nm (Fig. 22(a)) and 1000 nm (Fig. 22(b)), respectively. The latter excitation conditions correspond either to photon energies larger than or less than $E_g/2$ (for ZnS with $E_g = 2.7$ eV). The sign of the refractive index $\Delta n$ is discriminated based on the specific shape of the *Z*-scan transmittance curve.

A positive refractive index change is identified when the normalized transmittance increases as the sample approaches the beam focus and decreases as it moves away from the focus, whereas a negative refractive index change produces the opposite behaviour. The extracted values of the refractive index for the *Z*-scans shown in Fig. 23 are $\Delta n = 2.8 \times 10^{-5}$ for the negative refraction case (Fig. 22(a)) and $\Delta n = 2.2 \times 10^{-4}$ for the positive refraction case (Fig. 22(b)), obtained at irradiance values of 1.7 GW/cm$^2$ and 8.8 GW/cm$^2$, respectively. The irradiance-dependent *Z*-scan results are relevant for comparison with the refraction profile mapping data of the present study to verify magnitude and sign of the $\Delta n$ irradiance dependent changes.

### *4.8. Analysis of the induced refractive index dependence on irradiance by comparing the results of Z-scan and self-refraction mapping*

The irradiance-dependent refractive index modulation $\Delta n$ values in ZnSe are summarized in Fig. 23. These values have been extracted by using three complementary experimental techniques, namely, area-integrated Z-scan measurements, spatially resolved self-refraction beam shaping analysis, and the pump-probe refraction mapping.

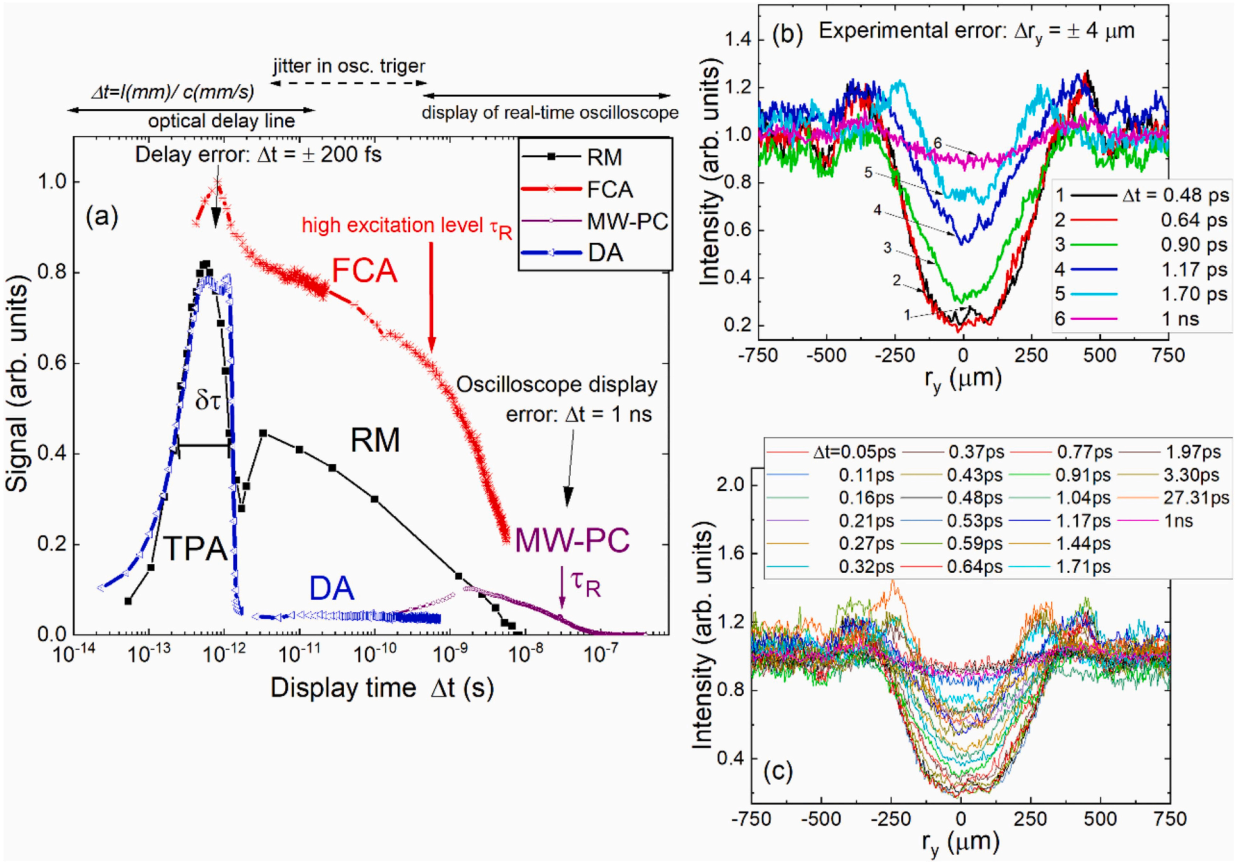


**Fig. 21.** (a) Experimentally recorded temporal dynamics of the pump-probe refraction mapping (RM), differential absorption (DA), microwave-probed photoconductivity (MW-PC), and free-carrier absorption (FCA) signals in ZnSe. The RM signal was transformed to the inverse differential intensity $-dI$, using probe beam profiles shown in (b) and (c), measured at the centre of the refracted beam, in order to get characteristics with comparable regions of signal increase and decrease. The MW-PC transient was measured at a relatively low excitation level ($\Delta N_{eh} \sim 10^{16}$ cm$^{-3}$), whereas the FCA relaxation transient was recorded under high excitation conditions ($\Delta N_{eh} \sim 10^{18}$ cm$^{-3}$). The comparison of the temporal responses highlights the correlation between refractive beam reshaping and photogenerated carrier dynamics. (b) The delay time dependent radial irradiance distribution profiles of the refracted probe beam illustrate the evolution of the ring-shaped beam structuring scaled with pump-probe delay scanning. (c) Complete set of RM transients used for reconstruction of the temporally evolving refraction mapping profiles.

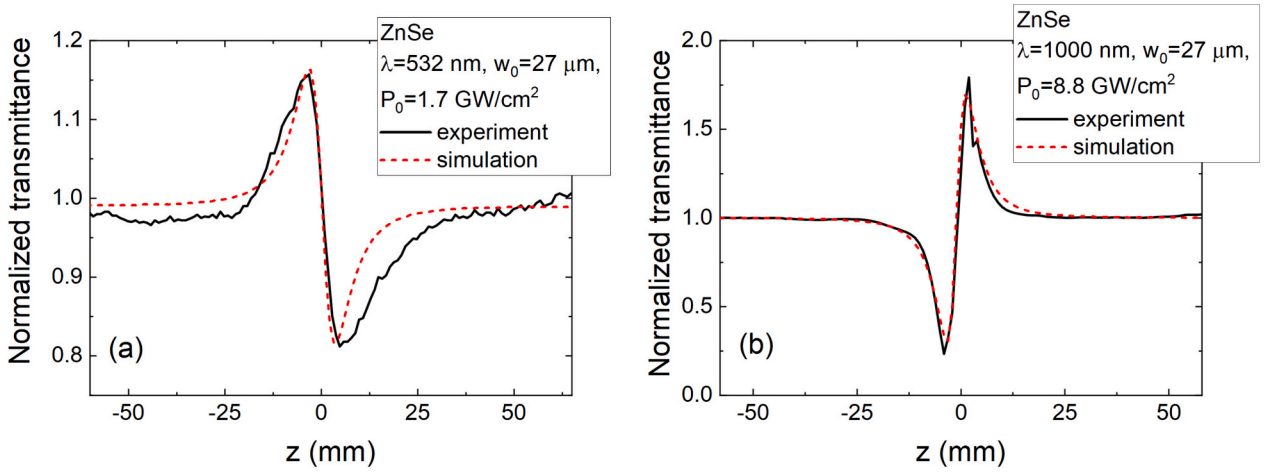


**Fig. 22.** Closed-aperture Z-scan transmittance curves measured (solid curves) and simulated (dashed curves) for a 3 mm thick ZnSe crystal at different excitation wavelengths: (a) 532 nm and (b) 1000 nm. The plotted curves represent the normalized transmitted intensity as a function of the sample position relative to the focal plane of the laser beam. The asymmetry and peak-valley characteristics of the transmittance curves were used to determine the sign and magnitude of the nonlinear refractive index $\Delta n$. The measurements at 532 nm and 1000 nm correspond to excitation photon energies above and below $E_g/2$, respectively, illustrating the wavelength-dependent $\Delta n$ sign in ZnSe.

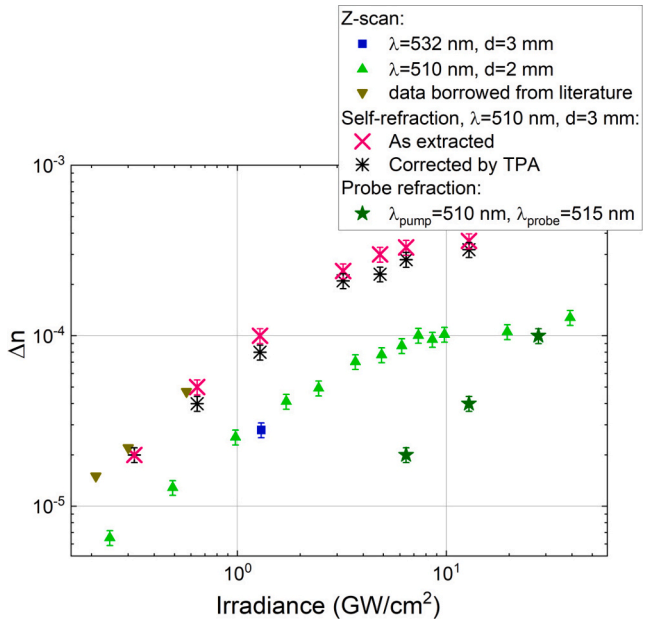


**Fig. 23.** Irradiance dependence of the refractive index modulation $\Delta n$ in ZnSe extracted using different experimental techniques and analysis approaches. Blue square represents $\Delta n$ value obtained by Z-scan measurements at $\lambda = 532$ nm using a 3 mm thick ZnSe sample. Green upward triangles correspond to Z-scan measurements performed at $\lambda = 510$ nm for a 2 mm thick ZnSe sample. Dark yellow downward triangles indicate $\Delta n$ values borrowed from literature (Sheik-Bahae et al., 1990). Magenta crosses show $\Delta n$ values extracted directly from self-refraction beam-profile fitting at $\lambda = 510$ nm using a 3 mm thick sample, while black asterisks represent the corresponding values after correction for two-photon absorption (TPA). Green stars correspond to $\Delta n$ values obtained in the pump-probe refraction-mapping regime using a pump wavelength of $\lambda_{pump} = 510$ nm and a probe wavelength of $\lambda_{probe} = 515$ nm. The comparison demonstrates the overall consistency of the irradiance-dependent nonlinear refraction characteristics obtained using local beam profile mapping and area-integrated Z-scan measurements, while also revealing systematic differences associated with distinct probing geometries and excitation conditions. (For interpretation of the references to colour in this figure legend, the reader is referred to the web version of this article.)

Despite fundamental differences in probing geometry and spatial sensitivity, all methods reveal a consistent monotonic increase of $\Delta n$ with increasing irradiance over more than two orders of magnitude. The experimentally extracted dependence of $\Delta n$ on irradiance (Fig. 23) remains approximately linear within the range of the correlated $\Delta n$-irradiance function. This suggests that the overall nonlinear refractive response remains predominantly governed by an effective third-order nonlinearity, while free-carrier generation contributes mainly to the temporal dynamics and magnitude of the refractive modulation observed in the pump-probe experiments. The values of $\Delta n$ extracted from self-refraction measurements show good agreement with the $Z$-scan results, particularly after correction for two-photon absorption, hinting that nonlinear absorption influences beam-profile-based extraction at elevated irradiance. These results are in line with those published in Ref. (Sheik-Bahae et al., 1990) and plotted in Fig. 23 for comparison. The pump-probe refraction results, however, exhibit lower $\Delta n$ values in comparison with the $Z$-scan and self-refraction-based results. These differences are expected because the employed techniques probe different aspects of the nonlinear optical response. The self-refraction measurements are highly sensitive to local refractive index gradients within the central high-irradiance region of the Gaussian excitation beam. In contrast, the pump-probe configuration employs a broad, weak probe beam that approaches the plane-wave approximation, resulting in partial spatial averaging of the induced refractive index distribution. The $Z$-scan technique provides an effective area-integrated nonlinear refractive response averaged over the entire beam cross-section and propagation path through the sample, making an addition to $\Delta n$ value due to integral over peripheral refraction beam area. Consequently, exact quantitative agreement between these methods is not necessarily expected. Additional differences may arise from variations in excitation wavelength, sample thickness, and probing geometry. Since the investigated wavelengths are located close to the spectral region where two-photon absorption and carrier-induced nonlinearities become significant in ZnSe, the nonlinear refractive response may exhibit strong spectral dependence. Moreover, the use of different sample thicknesses affects the accumulated nonlinear phase shift and free-carrier contribution to $\Delta n$ when $Z$-scan technique is applied. Possible systematic uncertainties associated with the fitting and modelling procedures should also be considered. These include sensitivity to the beam waist radius determination, correction for two-photon absorption radial distribution, detector noise, and the paraxial approximation assumptions employed in the simulations. Nevertheless, despite these limitations, the consistency of the observed irradiance-dependent trends across all methods supports the validity of the proposed refraction-mapping approach and confirms the role of carrier-induced nonlinear refraction in the investigated regime.

The experimentally extracted nonlinear refractive index changes in ZnSe are also consistent in sign and order of magnitude with previously reported literature data obtained using different nonlinear optical techniques. For example, nonlinear refractive index changes on the order of $10^{-4}$ at 532 nm and nanosecond laser pulses were reported using the Z-scan approach by Lee et al. (Lee et al., 1994), while time-resolved Z-scan measurements by Wang et al. (Said et al., 1992) yielded comparable values under picosecond excitation conditions. In the infrared spectral range, interferometric measurements at 1030 nm reported nonlinear refractive-index changes of approximately $2 \times 10^{-4}$ (Jansonas et al., 2022). The values obtained in the present work as a function of irradiance correlate with those reported in literature for the same general range despite differences in excitation wavelength, pulse duration, irradiance regime, temporal response, and measurement geometry. It should be noted that direct quantitative comparisons across studies are complicated by substantial variations in experimental conditions, including femtosecond versus nanosecond excitation, closed- versus open-aperture measurement configurations, and the relative contributions of instantaneous electronic and free-carrier nonlinearities. Nevertheless, the overall consistency of the obtained $\Delta n$ values with previously published data supports the validity of the proposed refraction-mapping approach and the interpretation of the observed beam-shaping phenomena in ZnSe.

### 4.9. Regimes of Gaussian beam shaping in laser technology applications

Consideration of limitations imposed by secondary focusing effects might be important in the formation of caustics due to light rays refracted by curved wave-fronts. The interplay between nonlinear refraction and absorption also complicates the analysis of planar intensity distribution integrals and, thereby, the separation of their parameters without evaluations of wave-front curvature modifications. The advanced developments of laser-based techniques, however, require deeper analysis of wave-front curvature modifications those cause wide-range changes of beam shape and irradiance.

The functional variations of the refracted beam divergence angle can be implemented by varying the magnitude of the negative refractive index with Gaussian radial distribution based on phenomena either of self-defocusing or pump-probe techniques implemented by the laser beam induced external refraction are illustrated in Fig. 24. It has been demonstrated that inhomogeneity of divergence angle profile leads to perturbations of the spread light beam shape, forming a ring in the limiting case, while the envelope of light rays, propagating within the central and periphery of the incident Gaussian beam may arrange a caustic of self-focused light at far-field distances. The radius of wave-

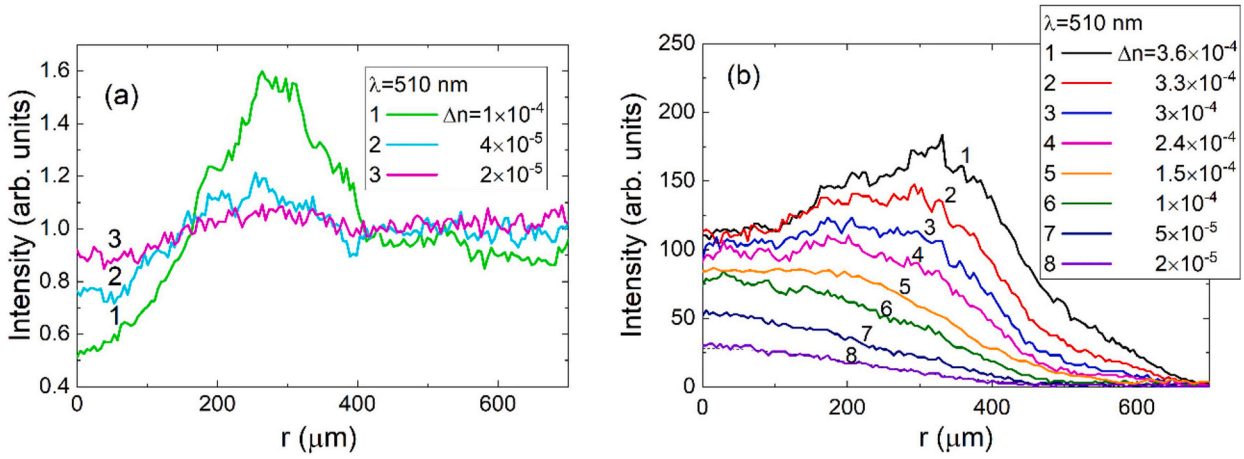


**Fig. 24.** (a) Formation of ring-shaped beams performed by combining varied intensity pulsed pump and wide probe beams, recorded by refraction profile mapping. There, the amplified irradiance of a rather sharply focused probe beam side can be obtained on the periphery of the pump beam. (b) Formation of a proper shape technological beam by choosing a suitable distance $L$ between the plane-parallel plate semiconductor shaper and the sample intended for laser ablation or patterning, as well as by varying the irradiance incident onto the semiconductor shaper.

front curvature, therefore, might change its sign within the lateral coordinates ($r$) of the incident Gaussian beam. Nevertheless, the developed model for predictably governed external refraction mapping and experimental verification of the structured beam lens-less formation makes groundings of the methodology for near-field laser technology.

These phenomena enable to make simple generators of ring-shaped beams of variable duration (up to ultrashort pulses) by lens-less manipulation of modulations of the refractive index in semiconductor plane-parallel beam shapers. However, the wave-front curvature-dependent phase shifts should be included within area integrals in further developments of structured beam technology when fluence integrated over the photon flux is recorded within the aperture of the photo-detector, making the description models more complicated.

## 5. Summary

A simple technique for externally induced Gaussian refractive index measurements based on 1D mapping of the transmitted irradiance profiles is presented. The assumption of the ray-optics model is based on curvature radius modifications under an induced gradient of refractive index. The validity of this model is limited by the Fresnel zone inherent in geometric optics. The structured light profiles cover shapes evolved from Gaussian to ring-like with the increase of incident irradiation and magnitude of the induced refractive index. The self-defocussing as well as the pump-probe regimes have been mainly examined. The models based on the ray-optics approach are described. The validity of the developed ray-optics model has been verified by mapping distances kept less than the Fresnel distance. The profiles of the ray divergence angle are related to the curvature radius determined by refractive index gradients. The validity of the paraxial approach is proved even for the case of declination from the Gaussian beam shape of spread light. The wave-front radius has been linked to this ray curvature based on mutually perpendicular parameters of the tangent and principal normal ascribed to the ray and wave-front curves. The validity of the simplified models has been verified by their coherence with experimental characteristics of the external refraction phenomena. The impact of diffraction and refraction angles has been analysed, and their relation with the total curvature radius has been determined. The radial and distance-dependent characteristics of the diffraction and refraction curvature radii for both positive and negative refractive indices have been derived, and different ranges for ray propagation have been revealed. The peculiarities of the externally induced refractive index measurements based on the analysis of transmitted beam shape variations dependent on the induced Gaussian profile waste radius $w_0$, on radial coordinate $r$ of the mapped 1D irradiance distribution, on sample thickness $d$, inherent distances $L$ and $L_{thr}$, and mainly on the magnitude of $\Delta n$. The applicability of the proposed technique for fast and direct evaluation of the material refractive index temporal and spectral characteristics is proved. It has been shown that the proposed technique can be employed by positioning the 1D video scanner in the range before the caustic zone. The distance of the caustic, measured from the plain-parallel sample (serving as a mask with an induced refractive index profile) to the mapping detector, has been additionally evaluated based on the intersection of the spread rays at the centre and the periphery of the induced Gaussian refractive index profile. In the case of defocusing, the threshold distance $L_{thr}$ of caustic appearance is related to the dimensionless width, as $(1 + L_{thr}\partial\Theta/\partial r) \leq 0$. The main features of the models and measurement modes have been verified and proven by combining several experimental techniques: 1D mapping of refracted beam profiles, simultaneous control of the two-photon absorption (TPA) temporal and spatial profile characteristics, simultaneous recording of the microwave-probed photoconductivity (MW-PC) transients, spectral and incident irradiance amplitude $Z$-scan characteristics. The rather good correlation of the incident/pump irradiance-dependent refractive index values, estimated using various refractive index mapping and Z-scan modes, has been obtained. Negative values of $\Delta n$ have been observed across the entire examined range of wavelengths and irradiances when refraction mapping and Z-scan correlations have been obtained. The self-focusing characteristics have been theoretically analysed in a brief research to illustrate the specifics of the ray-optics technique. The refraction profile mapping might be useful for deeper analysis of Z-scan characteristics, where beam profile changes might be important in the integrals of Z-scan signals. The pump-probe recording of the temporal cross-correlation of two-photon absorption as well as refraction beam profiling combined with delayed MW-PC transients, modified by excess-carrier decay, might serve as a technique of extremely temporal precision for the separation of competing mechanisms. Also, the time benchmark with ~1 ps resolution can be achieved by using the width of the cross-correlation peak within the pump-probe initial phase for the TPA and mapped refractive index profile variations. The simple and directly controlled method for the transmitted irradiance profiling by varying the incident beam intensity might serve as a technique for the lens-less beam shape modifications for laser-based ablation and micro-machining technologies. The structured light profiles obtained using the pump-probe refraction mappings directly demonstrate the irradiance-controlled potential of the lens-less temporal manipulations of

refracted structured light beams for laser technology purposes. In this research, the main aspects in validation of theoretical approach and experimental results have been demonstrated in such points: (i) the evolution of refracted beam shape from Gaussian one to structured light profile correspond to theoretically predicted changes of beam shape; (ii) the pump-probe refraction mappings obtained experimentally demonstrate an opportunity to amplify the plane wave beam by the induced changes of the refractive index profiles; (iii) the induced inhomogeneity of the TPA modifies the structured light profiles in the range of elevated irradiances; (iv) the clear correlation among refractive index modulation values and refractive index sign, estimated by developed techniques, confirms the prevailing mechanisms of the induced changes of material refraction characteristics and enables spectroscopy of these parameters in semiconductors; (v) validation of the developed ray optics model has been controlled by analysis of the caustic zone formation at distances below Fresnel one. Actually, the paraxial description is partially determined by Gaussian beams that induce refractive index gradients (the most strongly in the range of $0.7w_0$) within examined materials and plane-parallel samples. The Fresnel distance $L$ might be estimated using the waist radius $w_0$ of the incident Gaussian laser beam and the wavelength $\lambda$ of the mapping light, as $L \sim w_0^2/\lambda$. The methodology for refractive index measurements is based on mapping the evolution of beam shape control with gradual enhancement of the irradiance and the structured light profile corresponding to theoretically predicted changes of beam shape. The threshold distance $L_{thr}$ is estimated using the observation of the sharp ring-shape within recorded maps without further beam shape fragmentation due to interference effects. It should be noted that $L_{thr}$ depends on irradiance due to refractive index changes. Therefore, $L_{thr}$ is estimated for definite values of irradiance. This distance is evaluated by combining both self-refraction and probe-beam refraction regimes using the identical measurement conditions.

Only several typical characteristics have been considered in this article, as plenty of the experimental parameter sets can appear in practice, and their illustrations would be over-exuberant. Nevertheless, the presented methodology of ray optics might be useful in planning and preparing the material characterization and laser technology procedures. Also, this technique requires special choice and preparation of refraction material samples: mono-layered, speckle-less, with relevant band-gap and probe quantum ratio, with properly polished surfaces, inherent for commercially available ZnSe optical windows. The implementation of the measurement and technological regimes might be complicated due to the sensitivity of the method to the beam radius ($w_0$, $w(L)$), to the ratio of beam width and sample thickness ($w/d$), and distances between the refraction mask and the mapping plane ($L$, $L_{thr}$). The developed ray-optics technique might be applicable to the design of beam shapers when using Airy and other incident beams, different from Gaussian ones.

## CRediT authorship contribution statement

**Tomas Ceponis:** Writing – review & editing, Visualization, Supervision, Resources, Project administration, Methodology, Funding acquisition, Formal analysis. **Laimonas Deveikis:** Writing – review & editing, Visualization, Validation, Software, Investigation, Formal analysis, Data curation. **Kestutis Zilinskas:** Writing – review & editing, Visualization, Validation, Software, Investigation, Formal analysis, Data curation. **Eugenijus Gaubas:** Writing – review & editing, Writing – original draft, Supervision, Software, Project administration, Methodology, Formal analysis, Conceptualization.

## Declaration of competing interest

The authors declare that they have no known competing financial interests or personal relationships that could have appeared to influence the work reported in this paper.

## Acknowledgements

This project has received funding from the Research Council of Lithuania (LMTLT), agreement No. S-CERN-24-6.

## Data availability

Data will be made available on request.

## References

Akhmanov, S.A., Sukhorukov, A.P., Khokhlov, R.V., 1968. Self-focusing and diffraction of light in a nonlinear medium. Sov. Phys. Usp. 10, 609–636. https://doi.org/10.1070/PU1968v010n05ABEH005849.

Alda, J., 2015. Laser and Gaussian beam propagation and transformation. In: Encyclopedia of Optical and Photonic Engineering - Five Volume Set, second ed. CRC Press, Boca Raton. https://doi.org/10.1081/E-EOE2-120009751.

Boggess, T., Bohnert, K., Mansour, K., Moss, S., Boyd, I., Smirl, A., 1986. Simultaneous measurement of the two-photon coefficient and free-carrier cross section above the bandgap of crystalline silicon. IEEE J. Quantum Electron. 22, 360–368. https://doi.org/10.1109/JQE.1986.1072964.

Buono, W.T., Forbes, A., 2022. Nonlinear optics with structured light. Opto-Electron. Adv. 5, 210174. https://doi.org/10.29026/oea.2022.210174.

Catalano, I.M., Cingolani, A., Cingolani, R., Lepore, M., 1988. Interband two-photon absorption mechanisms in direct and indirect gap materials. Phys. Scr. 37, 579–582. https://doi.org/10.1088/0031-8949/37/4/014.

Cheng, J.L., Rioux, J., Sipe, J.E., 2011. Full band structure calculation of two-photon indirect absorption in bulk silicon. Appl. Phys. Lett. 98, 131101. https://doi.org/10.1063/1.3570654.

Cruz, C.D., Stephenson, J.C., Wahlstrand, J.K., 2024. Phase-sensitive pump-probe measurement of the complex nonlinear susceptibility of silicon across the direct band edge. Optica 11, 1313–1319. https://doi.org/10.1364/OPTICA.530147.

Dickey, F., 2000. Laser Beam Shaping: Theory and Techniques, second ed. CRC Press, Boca Raton. https://doi.org/10.1201/9780824741631.

Dinu, M., 2003. Dispersion of phonon-assisted nonresonant third-order nonlinearities. IEEE J. Quantum Electron. 39, 1498–1503. https://doi.org/10.1109/JQE.2003.818277.

Dresselhaus, M., Dresselhaus, G., Cronin, S.B., Gomes Souza Filho, A., 2018. Drude theory - free carrier contribution to the optical properties. In: Solid State Properties. Springer, Berlin, Heidelberg.

Eichler, H.-J., Günter, P., Pohl, D.W., 1986. Laser-Induced Dynamic Gratings. Springer, Berlin, Heidelberg.

Garcia, H., 2006. Tunneling assisted two-photon absorption: the nonlinear Franz-Keldysh effect. Phys. Rev. B 74, 035212. https://doi.org/10.1103/PhysRevB.74.035212.

Garcia, H., Avanaki, K.N., 2012. Direct and indirect two-photon absorption in Ge within the effective mass approximation. Appl. Phys. Lett. 100, 131105. https://doi.org/10.1063/1.3693389.

Garcia, H., Kalynamaran, R., 2006. Phonon-assisted two-photon absorption in the presence of a DC-field: the nonlinear Franz-Keldysh effect in indirect gap semiconductors, 2006 Conference on Lasers and Electro-Optics and 2006 Quantum Electronics and Laser Science Conference. IEEE, Long Beach, CA, USA, pp. 1–2. https://doi.org/10.1109/CLEO.2006.4628477.

Gaubas, E., Simoen, E., Vanhellemont, J., 2016. Review—carrier lifetime spectroscopy for defect characterization in semiconductor materials and devices. ECS J. Solid State Sci. Technol. 5, P3108–P3137. https://doi.org/10.1149/2.0201604jss.

Hadi, M., Deta, U.A., Husein, A.S., 2021. Linear and non-linear refractive indices in curved space. J. Phys. Conf. Ser. 1796, 012125. https://doi.org/10.1088/1742-6596/1796/1/012125.

Hutchings, D.C., Sheik-Bahae, M., Hagan, D.J., Van Stryland, E.W., 1992. Kramers-Krönig relations in nonlinear optics. Opt. Quant. Electron. 24, 1–30. https://doi.org/10.1007/BF01234275.

Ihrke, I., Ziegler, G., Tevs, A., Theobalt, C., Magnor, M., Seidel, H.-P., 2007. Eikonal rendering: efficient light transport in refractive objects. ACM SIGGRAPH 2007 Papers. https://doi.org/10.1145/1275808.1276451. , p. 59.

Jansonas, G., Budriunas, R., Vengris, M., Varanavicius, A., 2022. Interferometric measurements of nonlinear refractive index in the infrared spectral range. Opt. Express 30, 30507. https://doi.org/10.1364/OE.458850.

Kagawa, T., 2012. Two-photon absorption in photodiodes. In: Yun, I. (Ed.), Photodiodes - From Fundamentals to Applications. InTech, pp. 3–26. https://doi.org/10.5772/50491.

Khonina, S.N., Kazanskiy, N.L., Khorin, P.A., Butt, M.A., 2021. Modern types of axicons: new functions and applications. Sensors 21, 6690. https://doi.org/10.3390/s21196690.

Kovalev, M., Gritsenko, I., Stsepuro, N., Nosov, P., Krasin, G., Kudryashov, S., 2022. Reconstructing the spatial parameters of a laser beam using the transport-of-intensity equation. Sensors 22, 1765. https://doi.org/10.3390/s22051765.

Krauss-Kodytek, L., Ruppert, C., Betz, M., 2021. Near-infrared non-degenerate two-photon absorption coefficients of bulk GaAs and Si. Opt. Express 29, 34522. https://doi.org/10.1364/OE.433953.

Landau, L.D., Lifshtz, E.M., Pitaevskij, L.P., 1984. Electrodynamics of Continuous Media, second ed. Elsevier Butterworth-Heinemann, Amsterdam.

Laskin, A., Laskin, V., Ostrun, A., 2016. Refractive beam shapers for focused laser beams. Proc. SPIE 9950, 995002. https://doi.org/10.1117/12.2235712.

Lee, K.-H., Cho, W.-R., Park, J.-H., Kim, J.-S., Park, S.-H., Kim, U., 1994. Measurement of free-carrier nonlinearities in ZnSe based on the Z-scan technique with a nanosecond laser. Opt. Lett. 19, 1116–1118. https://doi.org/10.1364/OL.19.001116.

Madrid, J.A., 2008. A geometrical approach to time evolving wave fronts. Geophys. J. Int. 172, 1117–1122. https://doi.org/10.1111/j.1365-246X.2007.03699.x.

Minhaeng, C., 2025. Time-resolved nonlinear microspectroscopy with Gaussian beams. J. Chem. Phys. 162, 124201. https://doi.org/10.1063/5.0256032.

Pidgeon, C.R., Wherrett, B.S., Johnston, A.M., Dempsey, J., Miller, A., 1979. Two-photon absorption in zinc-blende semiconductors. Phys. Rev. Lett. 42, 1785–1788. https://doi.org/10.1103/PhysRevLett.42.1785.

Reddy, S.G., Kumar, A., Prabhakar, S., Singh, R.P., 2013. Experimental generation of ring-shaped beams with random sources. Opt. Lett. 38, 4441. https://doi.org/10.1364/OL.38.004441.

Rice, P., 2020. Classical electromagnetism and linear optics. In: An Introduction to Quantum Optics. IOP Publishing, Bristol. https://doi.org/10.1088/978-0-7503-1713-9ch2.

Sachleen, S., Forbes, A., 2026. Progress in structured light with nonlinear optics. Prog. Electromagn. Res. 185, 1–16. https://doi.org/10.2528/PIER25110804.

Said, A.A., Sheik-Bahae, M., Hagan, D.J., Wei, T.H., Wang, J., Young, J., Van Stryland, E. W., 1992. Determination of bound-electronic and free-carrier nonlinearities in ZnSe, GaAs, CdTe, and ZnTe. J. Opt. Soc. Am. B 9, 405. https://doi.org/10.1364/JOSAB.9.000405.

Saleh, B.E.A., Teich, M.C., 2019. Fundamentals of Photonics, third ed. Wiley, Hoboken.

Schmidt, M., Cvecek, K., Duflou, J., Vollersten, F., Arnold, C.B., Matthews, M.J., 2024. Dynamic beam shaping-improving laser materials processing via feature synchronous energy coupling. CIRP Ann-Manuf. Technol. 73, 533–559. https://doi.org/10.1016/j.cirp.2024.05.005.

Sharma, D., Gaur, P., Pal Malik, B., Singh, N., Gaur, A., 2012. Intensity dependent nonlinear absorption in direct and indirect band gap crystals under nano and picosecond Z-scan. OPJ 02, 98–104. https://doi.org/10.4236/opj.2012.22013.

Sheik-Bahae, M., Said, A.A., Wei, T.-H., Hagan, D.J., Van Stryland, E.W., 1990. Sensitive measurement of optical nonlinearities using a single beam. IEEE J. Quantum Electron. 26, 760–769. https://doi.org/10.1109/3.53394.

Sheik-Bahae, M., Said, A., Hagan, D., Soileau, M., Van Stryland, E., 1991a. Nonlinear refraction and optical limiting in thick media. Opt. Eng. 30, 1228–1235.

Sheik-Bahae, M., Hutchings, D.C., Hagan, D.J., Van Stryland, E.W., 1991b. Dispersion of bound electron nonlinear refraction in solids. IEEE J. Quantum Electron. 27, 1296–1309. https://doi.org/10.1109/3.89946.

Sheik-Bahae, M., Wang, J., Van Stryland, E.W., 1994. Nondegenerate optical Kerr effect in semiconductors. IEEE J. Quantum Electron. 30, 249–255. https://doi.org/10.1109/3.283767.

Soltani, M., Soref, R., 2015. Free-carrier electrorefraction and electroabsorption in wurtzite GaN. Opt. Express 23, 24984. https://doi.org/10.1364/OE.23.024984.

Tu, C., Wang, Q., Ren, Z.C., Wang, X.-L., Li, Y., Wang, H.-T., 2026. Advances in nonlinear manipulation of structured light fields: from fundamentals to applications. Light Manip. Appl. 1, 202506. https://doi.org/10.70401/lma.2026.0005.

Vaitkus, J., Gaubas, E., Kulevicius, C., 1986a. Non-linear refraction of two-dimensional laser beams in semiconductors. Lith. J. Phys. 26, 77–86.

Vaitkus, J., Jarasiunas, K., Gaubas, E., Jonikas, L., Pranaitis, R., Subacius, L., 1986b. The diffraction of light by transient gratings in crystalline, ion-implanted, and amorphous silicon. IEEE J. Quantum Electron. 22, 1298–1305.

Vaitkus, J., Gaubas, E., Kulevicius, C., Kapturauskas, J., 1987. External defocusing of laser beams in semiconductors. Lith. J. Phys. 27, 476–487.

Van Stryland, E.W., Vanherzeele, H., Woodall, M.A., Soileau, M.J., Smirl, A.L., Guha, S., Boggess, T.F., 1985. Two photon absorption, nonlinear refraction, and optical limiting in semiconductors. Opt. Eng. 24, 613. https://doi.org/10.1117/12.7973538.

Wherrett, B.S., 1984. Scaling rules for multiphoton interband absorption in semiconductors. J. Opt. Soc. Am. B 1, 67. https://doi.org/10.1364/JOSAB.1.000067.

Yan, C., Shiliang, P., Mingming, H., Linhan, L., Sitan, L., DaPeng, L., Fei, Y., 2025. Lightweight and efficient beam-shaping metalens for converting Gaussian beams into 2D flat-top beams. Opt. Express 33, 11555–11573. https://doi.org/10.1364/OE.555456.

Zhao, F., Liu, F., Li, Y., Yuan, M., Yao, X., Wang, J., Ye, Z., Chen, L., Huang, L., Wang, P., Han, W., Meng, Z., 2026. DMD-based programmable beam shaping for optical potential engineering. Photonics 13, 372. https://doi.org/10.3390/photonics13040372.

Znak, P., 2019. Wavefront Curvatures: Dynamic Ray Focusing and Diffraction Classification. Dissertation. Universität Hamburg. https://ediss.sub.uni-hamburg.de/handle/ediss/6337.